https://doi.org/10.5194/egusphere-2026-6872
Preprint. Discussion started: 23 November 2026
© Author(s) 2026. CC BY 4.0 License.

Reconstructing global dayside thermospheric $\Sigma O/N_2$ from GNSS total electron content maps via physics-guided deep learning

Hongwei Gong[1], Hanxian Fang[2,*], Die Duan[2,*], Chao Xiao[2], Chenghao Li[1], Chuyue Zhou[1], Jintai Li[2], Hongtao Huang[2], Ganming Ren[2], and Han Wu[2]

[1]College of Meteorology and Oceanography, National University of Defense Technology, Changsha 410073, China
[2]College of Advanced Interdisciplinary Studies, National University of Defense Technology, Changsha 411073, China

Correspondence: Hanxian Fang (fanghx@nudt.edu.cn) and Die Duan (dduanpku@163.com)

Abstract. The column density ratio of atomic oxygen to molecular nitrogen ($\Sigma O/N_2$) is a key indicator of ionosphere–thermosphere coupling, yet existing far-ultraviolet remote sensing cannot provide continuous global dayside coverage: GUVI aboard TIMED yields sparse orbital strips, while GOLD images only one-third of the dayside disk. Here we present TEC2ON2, a physics-guided framework that reconstructs continuous global dayside $\Sigma O/N_2$ maps from GNSS TEC maps. It builds upon an analytic relation that links $\Sigma O/N_2$ to TEC and solar extreme ultraviolet radiation, guiding both input feature design and a soft constraint in the loss function. Trained on sixteen years (2008–2023) of GUVI observations, the model reproduces fully independent 2024–2025 observations with an $R^2 = 0.927$ and RMSE$= 0.071$, an 18.1 % RMSE reduction over the DNN without physics-guided features or the soft constraint, with the largest gains during geomagnetically disturbed periods. The SHAP analysis further shows a larger contribution of the physics-guided features under disturbed conditions. Validated against GOLD observations of 15 geomagnetic storms in 2024–2025, TEC2ON2 reproduces the storm-time $\Sigma O/N_2$ evolution with a correlation coefficient of 0.80 and a ROC-AUC of 0.94, better than DNN and NRLMSIS 2.1. In the SRON2NN NmF2 reconstruction task, replacing the daily-mean GUVI $\Sigma O/N_2$ input reduces the NmF2 RMSE by up to 11.0 % in the replacement subset under disturbed conditions. The resulting 1999–2025 product ($2.5^\circ \times 5^\circ$, 2-hour resolution) offers a new GNSS-based capability for representing relative variations in thermospheric $\Sigma O/N_2$.

1 Introduction

The ionospheric plasma density is governed by production and loss processes, together with transport and diffusion (Schunk and Nagy, 2018). The major production comes from photoionization of atomic oxygen (O), whereas the major loss comes from chemical reactions with the nitrogen molecules (N_2). Thus, the column density ratio of O to N_2 ($\Sigma O/N_2$) has been used as a convenient indicator of the degree of a thermospheric disturbance (Burns et al., 1995; Cai et al., 2020; Verkhoglyadova et al., 2014; Meier, 2021). Many studies have suggested that $\Sigma O/N_2$ exhibits pronounced seasonal variations and storm-time depletion (Blanchfield et al., 2025; Liou et al., 2005), thereby driving variations in key ionospheric parameters, such as electron density, the F2-layer peak electron density (NmF2), and total electron content (TEC) (Gong et al., 2026b). Therefore, $\Sigma O/N_2$

https://doi.org/10.5194/egusphere-2026-6872
Preprint. Discussion started: 23 November 2026
© Author(s) 2026. CC BY 4.0 License.

plays an important role in understanding the complex ionospheric–thermospheric (I–T) coupling system, ionospheric modeling, and space weather applications.

However, continuous global observations of dayside $\Sigma O/N_2$ remain unavailable. Currently, the most widely used $\Sigma O/N_2$ products are retrieved from far ultraviolet (FUV) airglow remote sensing observations (Meier, 2021; Evans et al., 1995). The thermospheric $\Sigma O/N_2$ ratio is defined as

$$\Sigma O/N_2 \equiv \frac{\int_{h_{17}}^{\infty} n_O \, dh}{\int_{h_{17}}^{\infty} n_{N_2} \, dh} = \frac{\Sigma O}{10^{17}\ \mathrm{cm}^{-2}}, \tag{1}$$

where h_{17} denotes the altitude at which the overhead N_2 column density (integrated from infinity down to h_{17}) equals $10^{17}\ \mathrm{cm}^{-2}$, and ΣO is the O column density above h_{17}. It can be derived from the intensity ratio of the excited photoelectron OI 135.6 nm emission band to the N_2 LBHS (Lyman–Birge–Hopfield short) emission band (Strickland et al., 1995). Missions including the Global-scale Observations of the Limb and Disk (GOLD), Ionospheric Connection Explorer (ICON), and Thermosphere–Ionosphere–Mesosphere Energetics and Dynamics (TIMED) adopt this technique to derive thermospheric $\Sigma O/N_2$. GOLD, in geostationary orbit since 2018, images approximately one-third of the dayside disk every 30 minutes, leaving the remaining two-thirds unobserved (Correira et al., 2021; Eastes et al., 2017); ICON, in low Earth orbit with an inclination of 27°, provides $\Sigma O/N_2$ measurements primarily within $\pm 27°$ latitude from October 2019 to November 2022 (Immel et al., 2023); and the Global Ultraviolet Imager (GUVI) instrument aboard TIMED, in a $\sim 74°$ inclination orbit, has provided $\Sigma O/N_2$ measurements since 2002, producing two-dimensional swath maps with near-global coverage within one day (Christensen et al., 2003). This scanning capability ended in December 2007 when the scan motor failed; since then, GUVI has operated in spectrograph (stare) mode with the mirror fixed at $\sim 47°$ from nadir, recording full spectra along a narrow along-track strip. Empirical models such as NRLMSIS 2.1 offer climatological estimates but often lack precision during geomagnetic disturbances (Emmert et al., 2022), while physics-based models like the Thermosphere–Ionosphere–Electrodynamics General Circulation Model (TIEGCM) (Qian et al., 2014; Richmond et al., 1992) simulate the underlying physics but face challenges in real-time forecasting and are computationally intensive. Therefore, a key limitation of current remote-sensing-based $\Sigma O/N_2$ products is their limited spatiotemporal coverage. Reconstructing reliable $\Sigma O/N_2$ maps from these sparse remote sensing products remains an open issue.

Global Navigation Satellite System (GNSS) observations offer a unique complementary source for this reconstruction task. GNSS-based ionospheric sounding is a well-established remote sensing technique: ground- and space-based GNSS receivers measure the ionosphere-induced propagation delay of microwave signals, from which the TEC along the line of sight is retrieved, and the International GNSS Service (IGS) has archived global TEC maps continuously since 1998 (Hernández-Pajares et al., 2009). Unlike the FUV airglow measurements, which sample only where and when the instrument points, GNSS TEC is a long-term, all-weather observational record with global coverage, making it an ideal information source for reconstructing the sparsely sampled FUV-derived products. TEC is physically linked to thermospheric composition: to leading order, dayside TEC reflects the balance between production proportional to the atomic oxygen column and loss controlled by molecular species, a relation that can be derived explicitly from the electron continuity equation (Sect. 2.1). This coupling suggests that

https://doi.org/10.5194/egusphere-2026-6872
Preprint. Discussion started: 23 November 2026
© Author(s) 2026. CC BY 4.0 License.



global TEC maps, together with their temporal and spatial derivatives and solar extreme ultraviolet radiation, carry recoverable information about dayside $\Sigma O/N_2$.

In recent years, machine learning (ML) and deep learning (DL) have demonstrated great capabilities in space weather modeling (Tang et al., 2024; Li et al., 2025a; Xia et al., 2026; Yang et al., 2026; Li et al., 2025b; Kaselimi et al., 2022) and data fusion tasks (Hou et al., 2025; Tulasi Ram et al., 2018; Sui et al., 2024). Compared with empirical models, which are essentially climatological and tend to smooth out event-specific variability, deep networks trained on long-term observational records can capture nonlinear responses under extreme conditions such as geomagnetic storms, and improve reconstruction accuracy (Gong et al., 2026b; Li et al., 2024; Gong et al., 2026c). Compared with physics-based general circulation models, deep networks are lightweight and computationally inexpensive: once trained, they produce global estimates within seconds, making them well suited for nowcasting and long-term reconstruction (Irrgang et al., 2021). Nevertheless, purely data-driven models can be difficult to interpret and may produce physically inconsistent predictions (Ma et al., 2024). These limitations have motivated growing efforts to embed physical knowledge into network design, so that physically plausible relations can guide feature construction (Gong et al., 2026b) and regularize model behavior. In remote sensing, such physics-guided learning has proven particularly effective for multi-source data fusion and retrieval under sparse sampling, where the physics of the observation process provides the bridge between heterogeneous sensors (Hou et al., 2025; Raissi et al., 2019; Sui et al., 2023).

In this work, we present TEC2ON2, a physics-guided deep learning framework that reconstructs continuous global dayside $\Sigma O/N_2$ maps from GNSS TEC maps. Trained on sixteen years (2008–2023) of TIMED/GUVI orbital observations aggregated onto $1^\circ \times 1^\circ \times 1\,\mathrm{min}$ grids, the model is evaluated on fully independent data from 2024–2025, a period of solar maximum, including the May 2024 superstorm. The main contributions are: (1) an interpretable spatiotemporal reconstruction framework that recovers continuous global dayside $\Sigma O/N_2$ maps by fusing sparse FUV (used as training references) with globally continuous GNSS TEC observations, thereby converting an indirect but spatially complete observable into a thermospheric $\Sigma O/N_2$ product; (2) a physics-guided design in which the continuity-equation-derived relation guides both feature construction and a soft constraint in the loss function, improving generalization under geomagnetically disturbed conditions; (3) a dedicated holdout validation of extreme geomagnetic storms against GOLD observations and GUVI daily-averaged products; and (4) a publicly released 1999–2025 reconstruction product.

2 Method and data

2.1 Physical relationship between thermospheric $\Sigma O/N_2$ and ionospheric TEC

In the dayside ionosphere, electrons are primarily produced by the photoionization of atomic oxygen (O) in the ionospheric F layer driven by solar radiation. The variation in electron density is governed by the continuity equation (Schunk and Nagy, 2018):

$$\frac{\partial N_e}{\partial t} = q - L - \nabla \cdot (N_e \boldsymbol{V}), \tag{2}$$

https://doi.org/10.5194/egusphere-2026-6872
Preprint. Discussion started: 23 November 2026
© Author(s) 2026. CC BY 4.0 License.

where N_e denotes the electron density, q is the electron production rate, L is the electron loss rate, and $\nabla \cdot (N_e \boldsymbol{V})$ represents transport effects due to plasma diffusion and drift. Most of the electrons in the ionosphere are concentrated in the F layer, where electrons are primarily produced by the photoionization of atomic oxygen (O) under solar radiation, so q can be expressed as

$$q \approx I_\infty \sigma_O e^{-\tau(h)} n_O(h), \tag{3}$$

where I_∞ is the solar radiation at the top of the ionosphere, σ_O is the photoionization cross-section of atomic oxygen, $e^{-\tau(h)}$ represents the attenuation of the incoming radiation by the overlying atmosphere, and h is the altitude. In the F layer of the ionosphere, the loss term (L) is predominantly controlled by charge exchange between atomic oxygen ion (O^+) and the molecular species O_2 and N_2. Hence L can be expressed as

$$L \approx \beta N_e = (k_1 n_{O_2} + k_2 n_{N_2}) N_e, \tag{4}$$

where β is the linear loss coefficient, n_{O_2} and n_{N_2} are the density of O_2 and N_2, and $k_1 = 2.1 \times 10^{-11}\ \mathrm{cm^3\,s^{-1}}$ and $k_2 = 1.2 \times 10^{-12}\ \mathrm{cm^3\,s^{-1}}$ are the reaction rates.

The transport term $\nabla \cdot (N_e \boldsymbol{V})$ involves both horizontal and vertical motions of electron density and can therefore be expressed as

$$\nabla \cdot (N_e \boldsymbol{V}) = \nabla_h \cdot (N_e \boldsymbol{U}) + \frac{\partial}{\partial h} (N_e \omega), \tag{5}$$

where $\boldsymbol{U}$ is the horizontal velocity and ω is the vertical velocity. We substitute Eqs. (3), (4), and (5) into Eq. (2) and integrate both sides over altitude to obtain Eq. (6):

$$\frac{\partial \mathrm{TEC}}{\partial t} = I_\infty \sigma_O \int_{h_0}^{\infty} e^{-\tau(h)} n_O(h)\,\mathrm{d}h - \int_{h_0}^{\infty} (k_1 n_{O_2} + k_2 n_{N_2}) N_e\,\mathrm{d}h - \int_{h_0}^{\infty} \left[\nabla_h \cdot (N_e \boldsymbol{U}) + \frac{\partial}{\partial h} (N_e \omega)\right] \mathrm{d}h, \tag{6}$$

where h_0 denotes the lower integration boundary. The first term on the right-hand side of Eq. (6) can further be written as Eq. (7):

$$I_\infty \sigma_O \int_{h_0}^{\infty} e^{-\tau(h)} n_O(h)\,\mathrm{d}h = I_\infty \sigma_O \eta_O \Sigma O, \tag{7}$$

where η_O denotes the mean transmission over the O column and ΣO is the total O column density. Under diffusive equilibrium, the altitude distributions of N_2 and O_2 can be approximated by exponential decays. Accordingly, the number densities of O_2 and N_2 relative to their densities at reference height h_0 can be expressed as follows:

$$n_s = n_s(h_0) e^{-(h-h_0)/H_s}, \tag{8}$$

where S denotes O_2 or N_2, n_s is the density of O_2 or N_2 at the height of h, $n_s(h_0)$ is the density of O_2 or N_2 at the height of h_0, and H_s is the scale height of O_2 or N_2. Thus, substituting Eq. (8) into the second term of the right-hand side of Eq. (6) yields

$$\int_{h_0}^{\infty} (k_1 n_{O_2} + k_2 n_{N_2}) N_e\,\mathrm{d}h = [k_1 \eta_{O_2} n_{O_2}(h_0) + k_2 \eta_{N_2} n_{N_2}(h_0)]\,\mathrm{TEC}, \tag{9}$$

https://doi.org/10.5194/egusphere-2026-6872
Preprint. Discussion started: 23 November 2026
© Author(s) 2026. CC BY 4.0 License.

where η_{O_2} and η_{N_2} are electron-density-weighted factors, defined in Eq. (10):

$$\eta_{O_2} = \frac{\int_{h_0}^{\infty} e^{-(h-h_0)/H_{O_2}} N_e \, dh}{\mathrm{TEC}}, \qquad \eta_{N_2} = \frac{\int_{h_0}^{\infty} e^{-(h-h_0)/H_{N_2}} N_e \, dh}{\mathrm{TEC}}. \tag{10}$$

In addition, integrating Eq. (8) over altitude yields the expressions for the column densities of O_2 and N_2, as shown in Eq. (11):

$$\Sigma N_s = \int_{h_0}^{\infty} n_s(h_0) e^{-(h-h_0)/H_s} \, dh = n_s(h_0) H_s. \tag{11}$$

Substituting Eq. (11) into Eq. (9) gives Eq. (12):

$$\int_{h_0}^{\infty} (k_1 n_{O_2} + k_2 n_{N_2}) N_e \, dh = \left[k_1 \eta_{O_2} \frac{\Sigma O_2}{H_{O_2}} + k_2 \eta_{N_2} \frac{\Sigma N_2}{H_{N_2}} \right] \mathrm{TEC}. \tag{12}$$

As for the third term on the right-hand side of Eq. (6), the vertical term can be expressed as Eq. (13):

$$\int_{h_0}^{\infty} \frac{\partial}{\partial h} (N_e \omega) \, dh = (N_e \omega)|_{\infty} - (N_e \omega)|_{h_0}. \tag{13}$$

Owing to the relatively low electron densities at the upper and lower boundaries of the ionosphere, Eq. (13) tends toward zero. Then, we introduce a TEC-weighted effective horizontal velocity U_{eff}, as shown in Eq. (14):

$$\boldsymbol{U}_{\mathrm{eff}} = \frac{\int_{h_0}^{\infty} N_e \boldsymbol{U} \, dh}{\int_{h_0}^{\infty} N_e \, dh}. \tag{14}$$

So, the transport term can be expressed as Eq. (15):

$$\int_{h_0}^{\infty} \left[\nabla_h \cdot (N_e \boldsymbol{U}) + \frac{\partial}{\partial h} (N_e \omega) \right] dh = \boldsymbol{U}_{\mathrm{eff}} \cdot \nabla_h \mathrm{TEC} + \mathrm{TEC} (\nabla_h \cdot \boldsymbol{U}_{\mathrm{eff}}), \tag{15}$$

where $\boldsymbol{U}_{\mathrm{eff}} \cdot \nabla_h \mathrm{TEC}$ is the TEC advection term and $\mathrm{TEC}(\nabla_h \cdot \boldsymbol{U}_{\mathrm{eff}})$ is the TEC divergence term. We substitute Eqs. (7), (12), and (15) into Eq. (6) to yield

$$\Sigma O/N_2 = \frac{\frac{\partial \mathrm{TEC}}{\partial t} + \boldsymbol{U}_{\mathrm{eff}} \cdot \nabla_h \mathrm{TEC} + \left[\nabla_h \cdot \boldsymbol{U}_{\mathrm{eff}} + \frac{k_1 \eta_{O_2} \Sigma O_2}{H_{O_2}} + \frac{k_2 \eta_{N_2} \Sigma N_2}{H_{N_2}} \right] \mathrm{TEC}}{I_{\infty} \sigma_O \eta_O \Sigma N_2}, \tag{16}$$

According to Eq. (16), we find that many factors can influence the thermospheric $\Sigma O/N_2$, including the temporal variation of TEC ($\partial \mathrm{TEC}/\partial t$), the horizontal gradient of TEC ($\nabla_h \mathrm{TEC}$), which can be decomposed into its zonal ($\partial \mathrm{TEC}/\partial x$) and meridional components ($\partial \mathrm{TEC}/\partial y$), TEC, ΣO_2, ΣN_2, solar radiation I_{∞}, the TEC-weighted effective horizontal velocity $\boldsymbol{U}_{\mathrm{eff}}$, and the scale heights of O_2 and N_2. However, many of these terms lack continuous and direct observations. Therefore, in this work, we adopt the more readily available TEC, $\partial \mathrm{TEC}/\partial t$, $\nabla_h \mathrm{TEC}$, and solar radiation data to enhance the reconstruction of thermospheric $\Sigma O/N_2$.

https://doi.org/10.5194/egusphere-2026-6872
Preprint. Discussion started: 23 November 2026
© Author(s) 2026. CC BY 4.0 License.

2.2 Data processing

2.2.1 TIMED/GUVI $\Sigma O/N_2$ data processing

The TIMED satellite was launched by NASA in December 2001. It orbits the Earth at an altitude of 625 km with an inclination of 74°. It carries the GUVI instrument, which measures the spectral intensity of FUV airglow across the 110–185 nm range in five selectable bands. From 2002 to December 2007, GUVI operated in imaging (cross-track scanning) mode, in which $\Sigma O/N_2$ was retrieved from the intensity ratio of two photometric channels (135.6 nm and N_2 LBHS) via a lookup table parameterized by solar zenith angle and viewing geometry (Christensen et al., 2003). Since the scan-motor failure in December 2007, GUVI has operated in spectrograph (stare) mode, recording full 120–181 nm spectra at a fixed look angle ($\sim$47° from nadir) along a narrow strip beneath the orbit (Kil et al., 2022). The imaging-mode and spectrograph-mode $\Sigma O/N_2$ products therefore differ in both retrieval approach and viewing geometry. To ensure an internally consistent dataset of $\Sigma O/N_2$, the data derived from imaging-mode observations (2002–2007) are excluded from model training.

The thermospheric $\Sigma O/N_2$ products can be accessed in NetCDF format at https://guvitimed.jhuapl.edu/. The NetCDF data provide orbital $\Sigma O/N_2$ and daily-mean interpolated $\Sigma O/N_2$ from 2008 to the present. In this study, orbit $\Sigma O/N_2$ data from 2008 to 2025 are adopted to reconstruct high-resolution (temporal and spatial) $\Sigma O/N_2$ maps. Fig. 1a shows the global distributions of orbit $\Sigma O/N_2$ data provided by GUVI for day 66 of 2010. Given the systematic errors associated with GUVI observations and retrievals, non-positive values of $\Sigma O/N_2$ are first removed, and the three-sigma criterion is subsequently applied for data quality control, as described in Eq. (17):

$$\mu - 3\sigma \leq X(\Sigma O/N_2) \leq \mu + 3\sigma, \tag{17}$$

where X denotes the values of $\Sigma O/N_2$, μ represents the mean of X, and σ is the standard deviation of X. After the above quality control, approximately 10 000 records were removed, leaving about 7.7×10^7 valid data points.

Given the dense sampling of $\Sigma O/N_2$ along the orbit, in order to further suppress $\Sigma O/N_2$ retrieval noise and reduce duplicated information, we aggregate the orbital records onto a uniform $1° \times 1° \times 1$ min spatiotemporal grid (a superobbing procedure): samples falling within the same cell and minute are averaged, with each record assigned to its grid-cell center. This reduces the dataset from 7.7×10^7 samples to 2.3×10^7 grid cells.

As shown in Fig. 1a, there is a low $\Sigma O/N_2$ region over southeastern South America (red dashed box), which is also called the South Atlantic Anomaly (SAA). The $\Sigma O/N_2$ data in the SAA are contaminated by MeV particles. This contamination is an instrumental systematic effect rather than a geophysical signal (Zhang et al., 2014). To maintain data integrity while reducing the influence of the data in the SAA region, we retain all valid $\Sigma O/N_2$ data and adopt a weighting scheme during model training (Sect. 2.3.3).

2.2.2 IGS TEC map processing

The IGS has developed the Global Ionosphere Map (GIM) in the IONEX format, which is archived for long-term preservation (Hernández-Pajares et al., 2009). The typical spatial resolution of the GIMs is 2.5° in latitude and 5° in longitude,

https://doi.org/10.5194/egusphere-2026-6872
Preprint. Discussion started: 23 November 2026
© Author(s) 2026. CC BY 4.0 License.

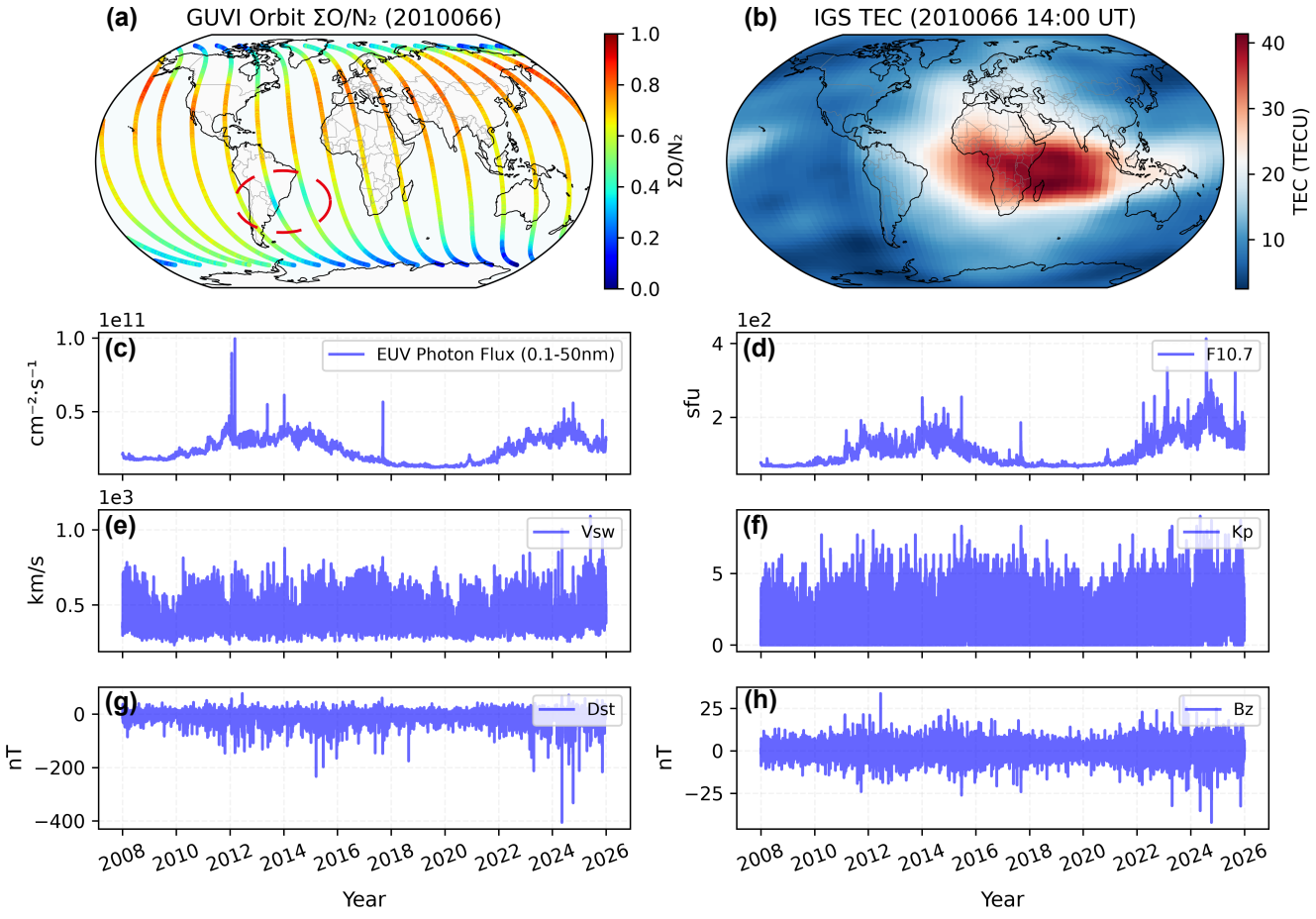

Figure 1. Input parameters from 2008 to 2025. (a) Orbit $\Sigma O/N_2$ distribution on day 66 of 2010; the red dashed elliptical box represents the SAA contamination region. (b) IGS TEC distribution at 14:00 UT (on day 66 of 2010). (c) EUV photon flux (0.1–50 nm), (d) F10.7 index, (e) V_{sw}, (f) Kp index, (g) Dst index, and (h) IMF B_z.

thus providing 71×73 grids globally. Currently, there are three main types of IGS GIM products including final, rapid, and predicted, and the final GIM has a more accurate ionosphere map compared to the other two types. The 2-hour resolution IGS GIMs feature long-term continuous records and serve as the primary TEC data product for long-term climatological analysis and ionospheric modeling. Accordingly, we adopt the 2-hour resolution final IGS GIMs (with the prefix "igsg") to obtain TEC values. The temporal variation rate and spatial gradients of TEC in Eq. (16) are approximately estimated from this dataset using the central difference method, as shown in Eq. (18), which are denoted as $\Delta\mathrm{TEC}_t$, the zonal gradient of TEC ($\Delta\mathrm{TEC}_x$), and

https://doi.org/10.5194/egusphere-2026-6872
Preprint. Discussion started: 23 November 2026
© Author(s) 2026. CC BY 4.0 License.

the meridional gradient of TEC ($\Delta\mathrm{TEC}_y$), respectively:

$$\begin{aligned}
\frac{\partial \mathrm{TEC}}{\partial t} &\approx \Delta\mathrm{TEC}_t = \frac{\mathrm{TEC}(t+2) - \mathrm{TEC}(t-2)}{4}, \\
\frac{\partial \mathrm{TEC}}{\partial x} &\approx \Delta\mathrm{TEC}_x = \frac{\mathrm{TEC}(\varphi, \lambda+\Delta\lambda) - \mathrm{TEC}(\varphi, \lambda-\Delta\lambda)}{2R_E \cos\varphi \Delta\lambda}, \\
\frac{\partial \mathrm{TEC}}{\partial y} &\approx \Delta\mathrm{TEC}_y = \frac{\mathrm{TEC}(\varphi+\Delta\varphi, \lambda) - \mathrm{TEC}(\varphi-\Delta\varphi, \lambda)}{2R_E \Delta\varphi},
\end{aligned} \tag{18}$$

where φ and λ denote geographic latitude and longitude, respectively. For IGS GIMs, the latitude interval ($\Delta\varphi$) is $2.5°$, and the longitude interval ($\Delta\lambda$) is $5°$. R_E denotes the mean Earth radius (6371 km). Fig. 1b shows the IGS GIMs at 14:00 for day 66 of 2010.

2.2.3 Solar radiation processing

According to Eq. (16), solar radiation I_∞ is also an important factor affecting $\Sigma O/N_2$. In this work, the 0.1–50 nm EUV radiation (I_{EUV}) provided by the Solar and Heliospheric Observatory's Solar EUV Monitor (SOHO/SEM) is used as a proxy for solar radiation, available from the LISIRD database (Judge et al., 1998). This band includes soft X-ray and short-wavelength EUV emissions, which are closely related to the photoionization processes responsible for daytime production of F-region plasma. In addition, the 0.1–50 nm flux dataset delivers stable, continuous records with relatively high temporal resolution over the study period, which is favorable for long-term model training. The original 15-second EUV measurements were averaged over 1-minute intervals to ensure temporal consistency with the superobbed $\Sigma O/N_2$. The 0.1–50 nm photon flux from 2008 to 2025 is shown in Fig. 1c.

2.2.4 Space weather indices

To capture the temporal dynamics of $\Sigma O/N_2$, we incorporate temporal features such as year, month, day, hour, and minute in Universal Time into our model. Furthermore, to account for the external forcing effects of solar and geomagnetic activities on $\Sigma O/N_2$, we incorporate multiple space weather indices in this study, including the solar and solar wind parameters like F10.7 and solar wind velocity (V_{sw}), geomagnetic indices (Kp, Dst), as well as the interplanetary magnetic field component B_z from the OMNI database (Papitashvili and King, 2020).

2.3 Methodology

2.3.1 Multilayer Perceptron (MLP) architecture

As indicated by Eq. (16), thermospheric $\Sigma O/N_2$ is influenced by TEC, the temporal variation of TEC, the horizontal gradient of TEC, solar EUV radiation, and atmospheric transport. However, several terms in the derived equation, such as the effective horizontal transport velocity, molecular column densities, and species-dependent scale heights are not continuously observed on a global scale. Therefore, an explicit analytical inversion of $\Sigma O/N_2$ from the available observations is difficult. In addition,

https://doi.org/10.5194/egusphere-2026-6872
Preprint. Discussion started: 23 November 2026
© Author(s) 2026. CC BY 4.0 License.

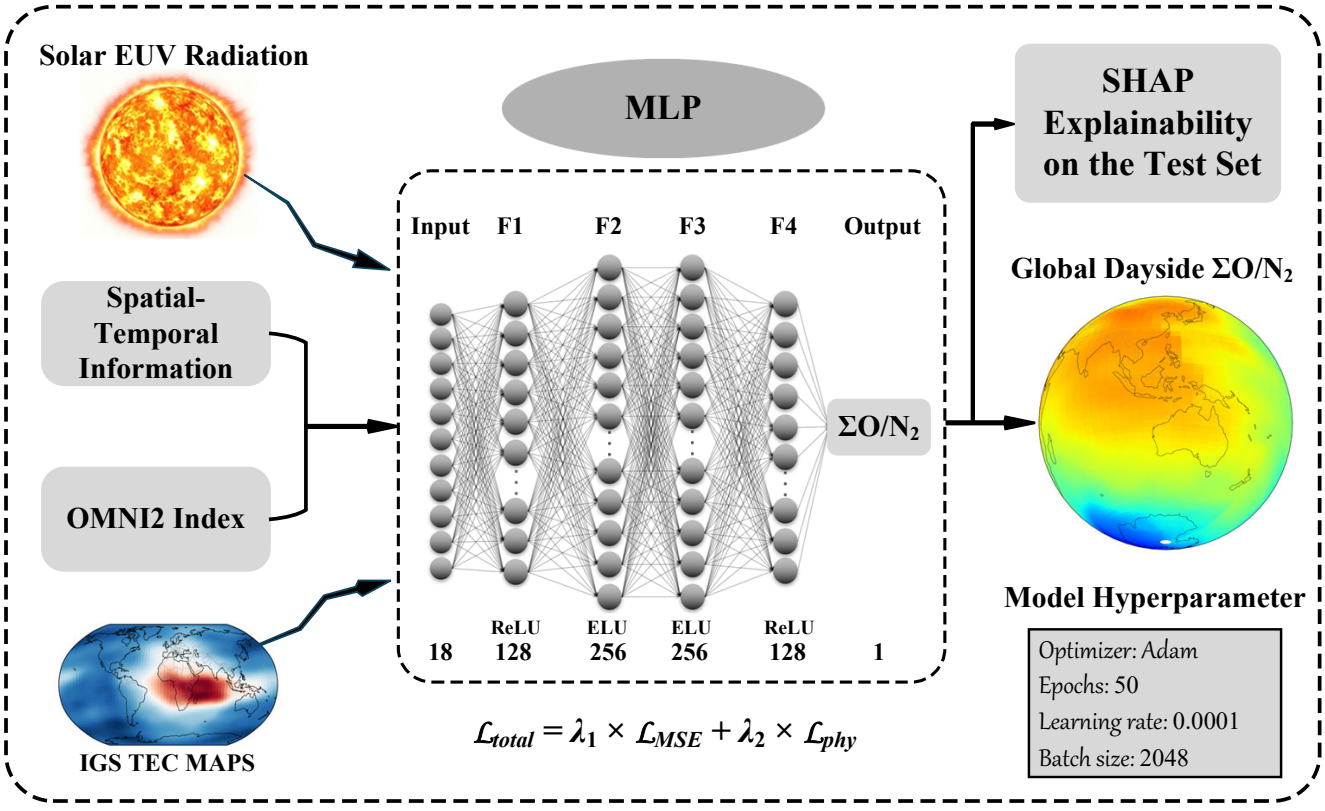

Figure 2. Architecture of the TEC2ON2 model.

the coupling among ionospheric plasma, thermospheric neutral composition, and solar radiation is highly nonlinear and cannot be adequately described by a simple linear regression.

To address this problem, we formulate the reconstruction of $\Sigma O/N_2$ as a supervised nonlinear regression problem and adopt a deep learning method, called TEC2ON2. It can be expressed as

$$\Sigma O/N_2(x, y, t) = f\left[x, y, \mathrm{sza}, \mathrm{TEC}, \Delta\mathrm{TEC}, \nabla_h \mathrm{TEC}, I_{\mathrm{EUV}}, \mathrm{F10.7}, V_{\mathrm{sw}}, \mathrm{Kp}, \mathrm{Dst}, B_z, t\right], \tag{19}$$

where x and y are geographical longitude and latitude, sza is the solar zenith angle, I_{EUV} denotes the observed solar EUV flux (0.1–50 nm), $\nabla_h \mathrm{TEC}$ can be decomposed into $\Delta\mathrm{TEC}_x$ and $\Delta\mathrm{TEC}_y$, and t represents the Universal Time variables including year, month, day, hour, and minute. Fig. 2 shows the architecture of TEC2ON2, which consists of sequential layers with 18, 128, 256, 256, 128, and 1 neurons. ReLU and ELU are employed as activation functions for the 1st/4th and 2nd/3rd hidden layers, respectively. The model was optimized using the Adam algorithm.

https://doi.org/10.5194/egusphere-2026-6872
Preprint. Discussion started: 23 November 2026
© Author(s) 2026. CC BY 4.0 License.

Table 1. The variation of the mean $\Sigma O/N_2$ deviation with the total geomagnetic field intensity.

Total field intensity (nT)	Samples	Deviation
21 000–22 000	176 954	−33.7 %
22 000–23 000	292 459	−17.2 %
23 000–24 000	402 977	−4.9 %
24 000–25 000	346 637	−0.3 %
25 000–28 000	705 566	2.4 %–4.5 %

2.3.2 Experimental setup

The full dataset from 2008 to 2025 was split into training (2008–2023) and test sets (2024–2025). The initial learning rate is set to 0.0001, the batch size to 2048, and the maximum number of epochs to 50. In order to validate the effectiveness of the physics-guided features introduced in TEC2ON2, SHapley Additive exPlanations (SHAP) values are computed to conduct a feature importance analysis of the trained TEC2ON2 model.

2.3.3 Loss function

This study proposes a two-branch loss function. The main loss function is the mean squared error (MSE) with respect to the orbital $\Sigma O/N_2$ observations, which is denoted as L_{MSE}. However, data in the SAA region are contaminated by MeV particles, leading to systematically low $\Sigma O/N_2$ values. To reduce the influence of these anomalous data on the model, each training sample is assigned a continuous credibility weight $w \in [0,1]$ before training. Specifically, the weight is derived from the geomagnetic field intensity provided by the International Geomagnetic Reference Field (IGRF). For each $\Sigma O/N_2$ point we evaluated the IGRF-13 total field intensity (F) at 150 km altitude, and quantified how the $\Sigma O/N_2$ deviation depends on F: for each 1000 nT wide bin of F, the mean $\Sigma O/N_2$ is compared with the value obtained in the same latitude (5°) and local time (2 h) bin but at $F \geq 30\,000$ nT. The results are summarized in Table 1.

As illustrated in Table 1, the deviation decreases toward zero as F approaches 24 000 nT, indicating that the contamination region can be confined to $F < 24\,000$ nT. A threshold of 24 000 nT is therefore adopted, and the weight is then defined as

$$w = \mathrm{clip}\left(\frac{F - 22\,000}{24\,000 - 22\,000}, 0, 1\right), \tag{20}$$

where $w = 0$ in the anomaly core ($F \leq 22\,000$ nT), $w = 1$ for $F \geq 24\,000$ nT, and w increases smoothly in between.

The main loss function L_{MSE} is then a weighted MSE:

$$L_{\mathrm{MSE}} = \frac{\sum_i w_i \left(\hat{y}_i - y_i\right)^2}{\sum_i w_i}, \tag{21}$$

where y_i represents the observed value, $\hat{y}_i$ represents the model output value, and w_i is the corresponding weight calculated by Eq. (20).

https://doi.org/10.5194/egusphere-2026-6872
Preprint. Discussion started: 23 November 2026
© Author(s) 2026. CC BY 4.0 License.

In addition, the explicit expression of $\Sigma O/N_2$ derived from Eq. (16) is incorporated into the loss function of the model as a soft constraint. However, many variables in Eq. (16) lack long-term continuous observational data. Therefore, only variables with long-term continuous observations, such as TEC, ΔTEC_t, ΔTEC_x, ΔTEC_y, and I_{EUV}, are adopted as features for the model. Subsequently, four learnable parameters (α, u, v, and γ) are introduced to replace the variables in Eq. (16) for which continuous observations are unavailable, as expressed in Eq. (22):

$$\begin{cases} \alpha = \dfrac{1}{\sigma_O \eta_O \Sigma N_2}, \quad u = U_{\text{eff}}^x, \quad v = U_{\text{eff}}^y, \\ \gamma = \dfrac{k_1 \eta_{O_2} \Sigma O_2}{H_{O_2}} + \dfrac{k_2 \eta_{N_2} \Sigma N_2}{H_{N_2}} + \nabla_h \cdot \boldsymbol{U}_{\text{eff}}. \end{cases} \tag{22}$$

Then, substituting the four learnable parameters and ΔTEC_t, ΔTEC_x, ΔTEC_y, and I_{EUV} into Eq. (16) yields

$$\Sigma O/N_2 = \frac{\alpha}{I_{EUV}} \left(\Delta TEC_t + u\,\Delta TEC_x + v\,\Delta TEC_y + \gamma\,TEC \right). \tag{23}$$

However, a least-squares fit between the results calculated by Eq. (23) and the observations in the training set shows that the outputs of Eq. (23) have a positive correlation trend with the training observations ($r \approx 0.52$). Nevertheless, the negative coefficient of determination indicates that Eq. (23) can constrain the variation direction of $\Sigma O/N_2$ to some extent, but fails to constrain the magnitude of its variations. We therefore define the correlation between the network output $\hat{y}$ and the physical-branch output $\hat{y}_{phy}$ for the physical branch. This term only constrains the consistency between $\hat{y}$ and $\hat{y}_{phy}$ in their spatiotemporal variability patterns, as formulated in Eq. (24):

$$L_{phy} = 1 - \text{Corr}\left(\hat{y}, \hat{y}_{phy}\right). \tag{24}$$

The total loss function is

$$L_{total} = \lambda_1 L_{MSE} + \lambda_2 \times L_{phy}, \tag{25}$$

where λ_1 and λ_2 are weight coefficients. During training, the L_{MSE} converges to approximately 0.08 while the L_{phy} converges to around 0.4. To balance the relative magnitudes of these two loss terms, we set the weight ratio $\lambda_1 : \lambda_2 = 5 : 1$.

2.3.4 Evaluation metrics

In the following section, we aim to validate and analyze the performance of the TEC2ON2 model for predicting the thermospheric $\Sigma O/N_2$ from different aspects, and several statistical metrics are selected, including root mean squared error (RMSE), mean absolute error (MAE), coefficient of determination (R^2), and Pearson correlation coefficient (CC). The equations are

https://doi.org/10.5194/egusphere-2026-6872
Preprint. Discussion started: 23 November 2026
© Author(s) 2026. CC BY 4.0 License.



defined as follows:

$$\begin{cases} \mathrm{CC} = \dfrac{\sum_{i=1}^{n}\left(y_i-\bar{y}\right)\left(\hat{y}_i-\bar{\hat{y}}\right)}{\sqrt{\sum_{i=1}^{n}\left(y_i-\bar{y}\right)^2}\sqrt{\sum_{i=1}^{n}\left(\hat{y}_i-\bar{\hat{y}}\right)^2}}, \\ \mathrm{RMSE} = \sqrt{\dfrac{1}{n}\sum_{i=1}^{n}\left(y_i-\hat{y}_i\right)^2}, \\ \mathrm{MAE} = \dfrac{1}{n}\sum_{i=1}^{n}\left|y_i-\hat{y}_i\right|, \\ R^2 = 1-\dfrac{\sum_{i=1}^{n}\left(y_i-\hat{y}_i\right)^2}{\sum_{i=1}^{n}\left(y_i-\bar{y}\right)^2}, \end{cases} \tag{26}$$

where y_i represents the observed value, $\hat{y}_i$ represents the model output value, $\bar{y}$ and $\bar{\hat{y}}$ are their respective means, and n is the number of samples.

3 Results and discussion

3.1 TEC2ON2 reconstruction result

3.1.1 Overall performance on the test set

Before model training, the data from 2024–2025 (the solar maximum period of Solar Cycle 25) were reserved as the test set and were not involved in model training or parameter optimization. We use this dataset to evaluate whether TEC2ON2 can reconstruct the key spatiotemporal variations of $\Sigma O/N_2$. Fig. 3 shows the $\Sigma O/N_2$ modeling results for TEC2ON2 across the entire test set, along with the corresponding TIMED/GUVI observations and NRLMSIS 2.1 outputs for comparison. The data were divided into four seasonal groups: spring (March–May), summer (June–August), autumn (September–November), and winter (December–February). The geographic coordinates of the depicted results span $90°$S to $90°$N in latitude and $180°$W to $180°$E in longitude, with a spatial resolution of $1°$ in both dimensions. Owing to the $\sim 74°$ orbital inclination of the TIMED satellite, data at high latitudes, especially near the polar regions, are missing.

As shown in Fig. 3, the seasonal and latitudinal–longitudinal variations of $\Sigma O/N_2$ from the TEC2ON2 model are in good agreement with TIMED/GUVI observations. The low-$\Sigma O/N_2$ feature over the SAA in the TIMED/GUVI observations has no counterpart in NRLMSIS 2.1; in the TEC2ON2 results (the middle column of Fig. 3), no significant SAA-related structure is evident either, which may reflect the down-weighting of SAA samples during model training. Nevertheless, the seasonal variations and spatial distributions of the three datasets show good consistency, indicating TEC2ON2's capability in capturing the spatiotemporal patterns of the thermospheric $\Sigma O/N_2$.

https://doi.org/10.5194/egusphere-2026-6872
Preprint. Discussion started: 23 November 2026
© Author(s) 2026. CC BY 4.0 License.

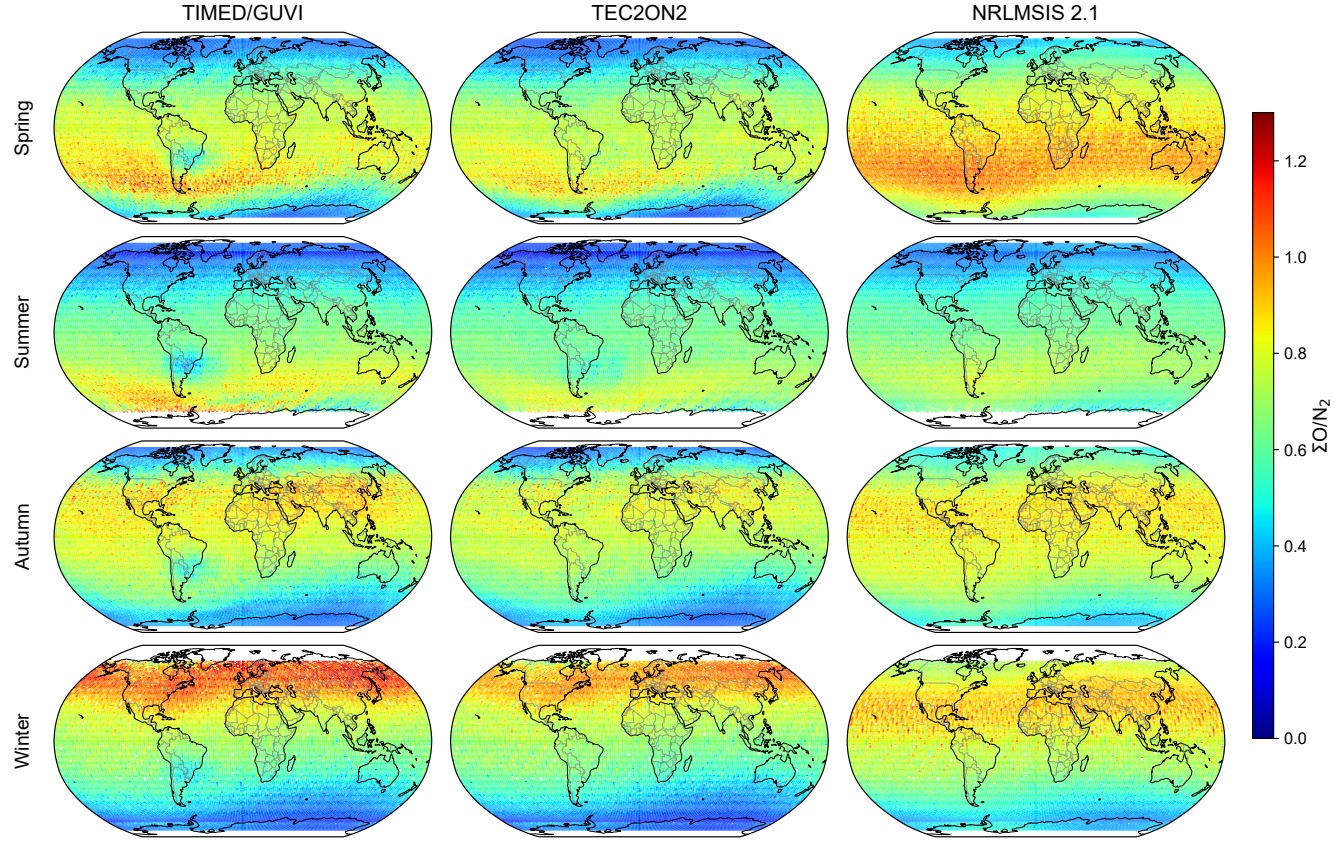

Figure 3. Geographic latitude and longitude variations of $\Sigma O/N_2$ across the test set (2024–2025). From left to right: TIMED/GUVI observations, TEC2ON2 predictions, and the corresponding NRLMSIS 2.1 output. From top to bottom: spring (March, April, May), summer (June, July, August), autumn (September, October, November), and winter (December, January, February).

3.1.2 Performance in geomagnetic quiet and disturbed periods

During geomagnetic storms, $\Sigma O/N_2$ shows prominent depletion due to polar energy injection, which further leads to severe variations in key ionospheric parameters such as electron density, peak electron density, and TEC. For the $\Sigma O/N_2$ reconstruction task, the reconstruction performance during geomagnetically disturbed periods is especially important. We therefore divide the test dataset (excluding the SAA region) into a geomagnetically quiet subset and a geomagnetically disturbed subset according to whether the Dst index is ≥ -30 nT or < -30 nT. Fig. 4 shows the density distributions of TEC2ON2-predicted versus TIMED/GUVI-observed $\Sigma O/N_2$. Fig. 4a and b show that the TEC2ON2 results are in good agreement with TIMED/GUVI observations. The $\Sigma O/N_2$ values are well distributed around the white dashed line. Aside from the slight underestimation of observed values by both subsets and the fact that evaluation metrics are slightly worse in disturbed periods than in quiet periods, the results generally align well with the observations.

https://doi.org/10.5194/egusphere-2026-6872
Preprint. Discussion started: 23 November 2026
© Author(s) 2026. CC BY 4.0 License.

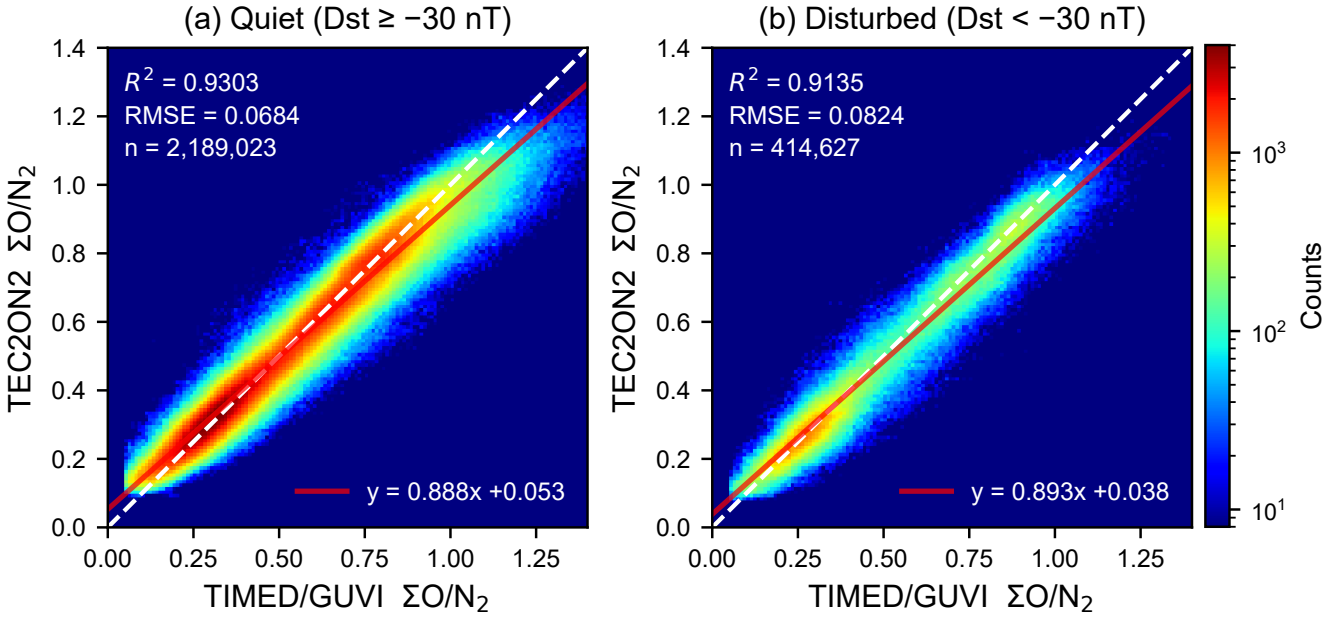

Figure 4. The white dashed line denotes the 1:1 relation; red lines are linear fits; (a) geomagnetically quiet (Dst ≥ -30 nT) and (b) geomagnetically disturbed (Dst < -30 nT).

3.1.3 The reconstruction error distribution

Fig. 5 summarizes the overall error of TEC2ON2 over the test set; panels (a)–(c) exclude the samples flagged as contaminated by the SAA, whereas the maps in (d)–(f) retain the full sample. The residuals of the TEC2ON2 model (i.e., reconstructed values minus observed values, Fig. 5a) yield a mean of -0.008 and a standard deviation of 0.07, corresponding to a central 95 % interval of $[-0.169, +0.108]$. The residual distribution presents a sharp peak with an excess kurtosis of 6.7 and weak skewness of -0.5. Such statistical characteristics demonstrate a favorable agreement between predicted and observed $\Sigma O/N_2$ values, with the majority of residuals concentrated around zero. The slight negative skewness indicates a slightly heavier negative tail, which corresponds to a small number of underestimated samples. Meanwhile, the near-zero residual mean verifies the absence of systematic bias in the model.

Figs. 5b and c show how the RMSE varies with geographic latitude and with the solar zenith angle. Since the 2024–2025 evaluation interval samples a different part of the $\Sigma O/N_2$ range from the training period, a systematic mismatch of the reconstruction is a priori more likely there, and it would remain indistinguishable from an increased sample-to-sample dispersion if only the RMSE were reported. We therefore separate the two parts of the RMSE according to Eq. (27):

$$\mathrm{RMSE}^2 = \mathrm{bias}^2 + \sigma_{\mathrm{eff}}^2, \tag{27}$$

where σ_{eff} denotes the random component.

https://doi.org/10.5194/egusphere-2026-6872
Preprint. Discussion started: 23 November 2026
© Author(s) 2026. CC BY 4.0 License.

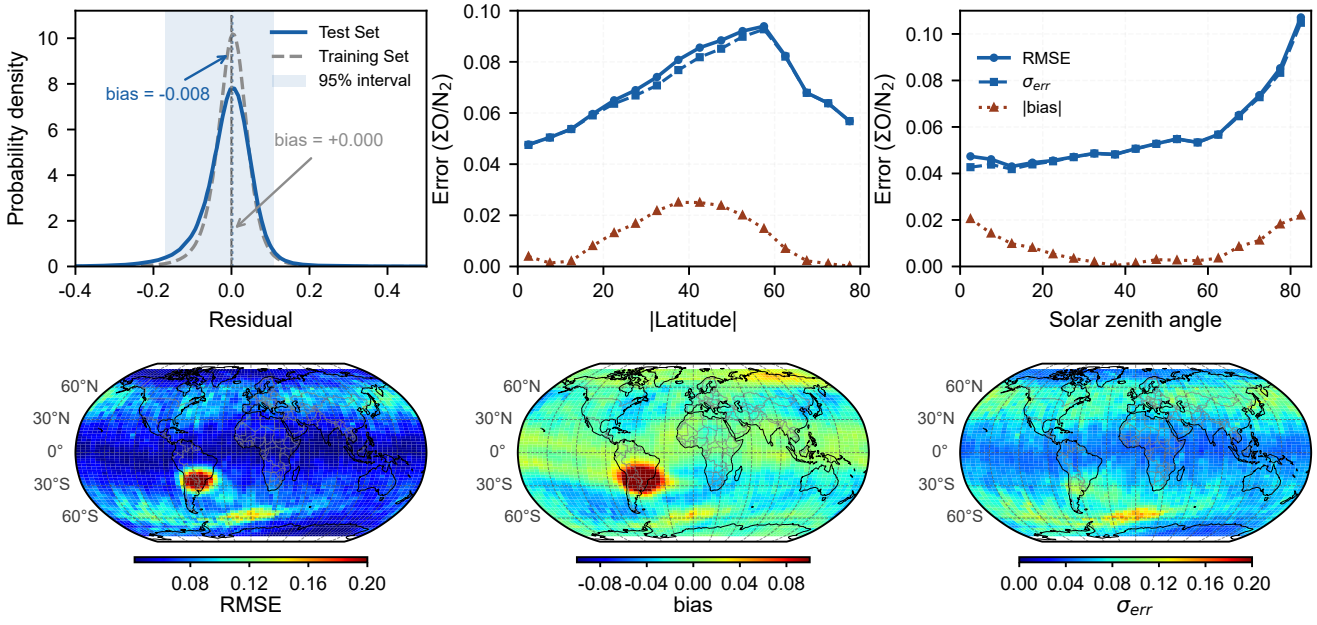

Figure 5. Error characteristics of the TEC2ON2 reconstruction of $\Sigma O/N_2$ over the test set. (a) The residual (TEC2ON2 predicted minus TIMED/GUVI observed); (b) the variation of the RMSE, bias, and random component σ_{eff} with latitude; (c) the variation of the RMSE, bias, and random component σ_{eff} with solar zenith angle; (d)–(f) global maps of the RMSE, the bias, and σ_{eff}.

Fig. 5b illustrates the latitude-dependent error characteristics. The RMSE increases steadily from low latitudes, peaks at $55°$–$60°$ (0.094, with $\sigma_{\text{eff}} = 0.0927$) and decreases again toward the polar range covered by the data (0.057 at $75°$–$80°$). The bias stays small everywhere—its magnitude stays below 0.026 in every band—and its share of the MSE peaks at $35°$–$40°$ with 9.6 %, against 0.7 % at $0°$–$5°$. The latitude dependence of the error is therefore a dependence of the σ_{eff}, not of the bias.

As for the solar zenith angle dependence (Fig. 5c), the minimum RMSE of 0.043 occurs at $10°$–$15°$, and the RMSE increases progressively toward larger angles, reaching 0.107 at $80°$–$85°$ (a factor of 2.5). Between $0°$ and $60°$ the RMSE stays within 0.043–0.056. The bias does not follow the same trend: its magnitude is U-shaped in the solar zenith angle, being largest at both ends of the range ($|\text{bias}| = 0.021$ in the $0°$–$5°$ and 0.022 at $80°$–$85°$) and smallest near $35°$–$40°$ (0.0004). Its relative weight is nevertheless dominated by the low-angle end, because the σ_{eff} grows much faster than the bias: bias^2 accounts for 18.7 % of the MSE in the $0°$–$5°$ and 4.2 % at $80°$–$85°$, and at most 0.5 % between $30°$ and $65°$.

Figs. 5d–f reveal the spatial patterns of the three errors. These maps use the full test set, including the SAA, so that the region affected by the down-weighting remains visible. The RMSE remains relatively uniform with a median value of 0.069 and exhibits a single peak of 0.249 within the SAA. The bias map flips its sign at this location and reaches $+0.229$ within the same grid cell, constituting a spatial footprint of the region-specific down-weighting adopted during model training. These SAA-associated values are reported for completeness only and are excluded from model ranking. Outside the SAA the median

https://doi.org/10.5194/egusphere-2026-6872
Preprint. Discussion started: 23 November 2026
© Author(s) 2026. CC BY 4.0 License.

Table 2. Feature and loss-function configurations and test-set performance of three MLP-based models.

Model name	Baseline features	Physics-guided features	L_{MSE}	L_{phy}	R^2	CC	RMSE	MAE
DNN	yes	no	yes	no	0.892	0.946	0.0864	0.0605
TECNN	yes	yes	yes	no	0.919	0.969	0.0744	0.0534
TEC2ON2	yes	yes	yes	yes	0.927	0.965	0.0708	0.0492

bias is only -0.001 against a median RMSE of 0.069, and the σ_{eff} map is nearly identical to the RMSE map, as expected from the fact that the bias accounts for at most 10 % of the MSE in any 5° latitude band (Fig. 5b).

These results demonstrate that the reconstruction performance is limited mainly by the random component, and larger errors occur at mid-latitudes and under high solar zenith angles.

3.2 The contribution of the physics-guided design

To further investigate the contributions of our physics-guided design to improving $\Sigma O/N_2$ reconstruction accuracy, we trained two additional configurations of the MLP architecture (DNN and TECNN). The feature and loss function configurations are shown in Table 2. The baseline configuration uses only the conventional geophysical drivers (F10.7, Kp, Dst, V_{sw}, B_z, solar zenith angle, and spatiotemporal coordinates), and a physics-guided configuration additionally incorporating TEC, $\Delta\mathrm{TEC}_t$, $\Delta\mathrm{TEC}_x$, $\Delta\mathrm{TEC}_y$, and the SOHO/SEM EUV radiation. The three models adopt identical training parameters and configurations, except for the feature setup and loss function.

3.2.1 The contribution of physics-guided features

The detailed feature setup and loss function of DNN and TECNN are shown in Table 2. On the entire test set, TECNN achieves better performance than DNN across all evaluation metrics. The RMSE is reduced by approximately 13.9 %, and the MAE decreases by around 11.7 %. To explore whether this improvement is robust during geomagnetic storms, we stratified the test set by the Dst index into four categories: $\mathrm{Dst} \geq -30$, $-50 \leq \mathrm{Dst} < -30$, $-100 \leq \mathrm{Dst} < -50$, and $\mathrm{Dst} < -100$. As shown in Fig. 6, the gain brought by the physics-guided features increases monotonically with geomagnetic activity. Relative to DNN, TECNN reduces the RMSE by 12.6 % for $\mathrm{Dst} \geq -30$ nT, 14.5 % for $-50 \leq \mathrm{Dst} < -30$ nT, 18.7 % for $-100 \leq \mathrm{Dst} < -50$ nT, and 29.2 % for $\mathrm{Dst} < -100$ nT, with corresponding MAE reductions of 11.2 %, 11.6 %, 16.8 %, and 27.7 %.

In addition, we computed SHAP values for TECNN and TEC2ON2 with a DeepExplainer, separately for the geomagnetic quiet ($\mathrm{Dst} \geq -30$ nT) and disturbed ($\mathrm{Dst} < -30$ nT) subsets (Fig. 7). The same background sample, drawn from the test set, was used for both subsets. As illustrated in Fig. 7, the five physics-guided features account for 25.2 % for TECNN and 30.6 % for TEC2ON2 of the total mean $|\mathrm{SHAP}|$ in the geomagnetically quiet conditions and 30.4 % for TECNN and 36.3 % for TEC2ON2 in the disturbed conditions. Most of this change stems from TEC itself, whose contribution share increases from 19.0 % to 24.0 % for TECNN and 20.0 % to 25.1 % for TEC2ON2, while the two dominant spatiotemporal features decline

https://doi.org/10.5194/egusphere-2026-6872
Preprint. Discussion started: 23 November 2026
© Author(s) 2026. CC BY 4.0 License.

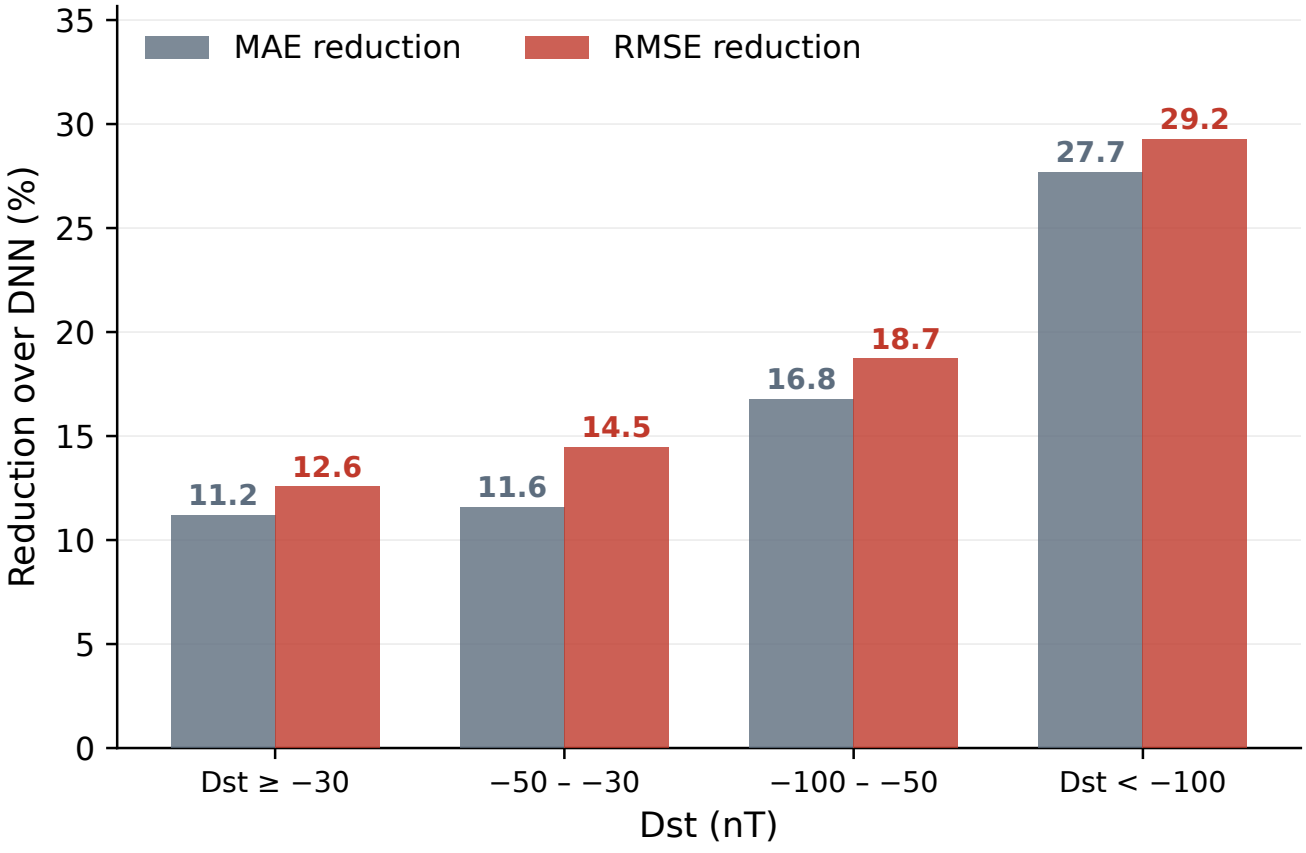

Figure 6. MAE and RMSE reductions of TECNN compared with DNN under different Dst index conditions. Reductions are defined as $100 \times (\mathrm{Metric}_{\mathrm{DNN}} - \mathrm{Metric}_{\mathrm{TECNN}})/\mathrm{Metric}_{\mathrm{DNN}}$ for the 2024–2025 test set, with positive values indicating improvement.

accordingly (latitude: from 23.0 % to 20.4 % for TECNN and from 21.0 % to 18.4 % for TEC2ON2; month: from 22.6 % to 18.4 % for TECNN and from 20.8 % to 17.3 % for TEC2ON2). Together with the ablation results, these findings indicate that the five physics-guided features we introduced play a greater role under disturbed conditions, consistent with the larger RMSE gains.

3.2.2 The contribution of the physics-guided soft constraint design

Many studies have shown that the $\Sigma O/N_2$ value is greater during solar maximum (Zhang and Paxton, 2011; Li et al., 2022). The test period covers the solar maximum phase and is fully outside the training window. As shown in Table 3, between the training period (2008–2023) and test period (2024–2025), the observed mean $\Sigma O/N_2$ increases from 0.447 to 0.528, representing an 18.1 % rise. The mean $\Sigma O/N_2$ predicted by the TECNN is 0.493, capturing only 56.8 % of this shift, and is therefore systematically low over the test period. The RMSE of TECNN is 0.0744, with a bias of -0.035 and a random component

https://doi.org/10.5194/egusphere-2026-6872
Preprint. Discussion started: 23 November 2026
© Author(s) 2026. CC BY 4.0 License.

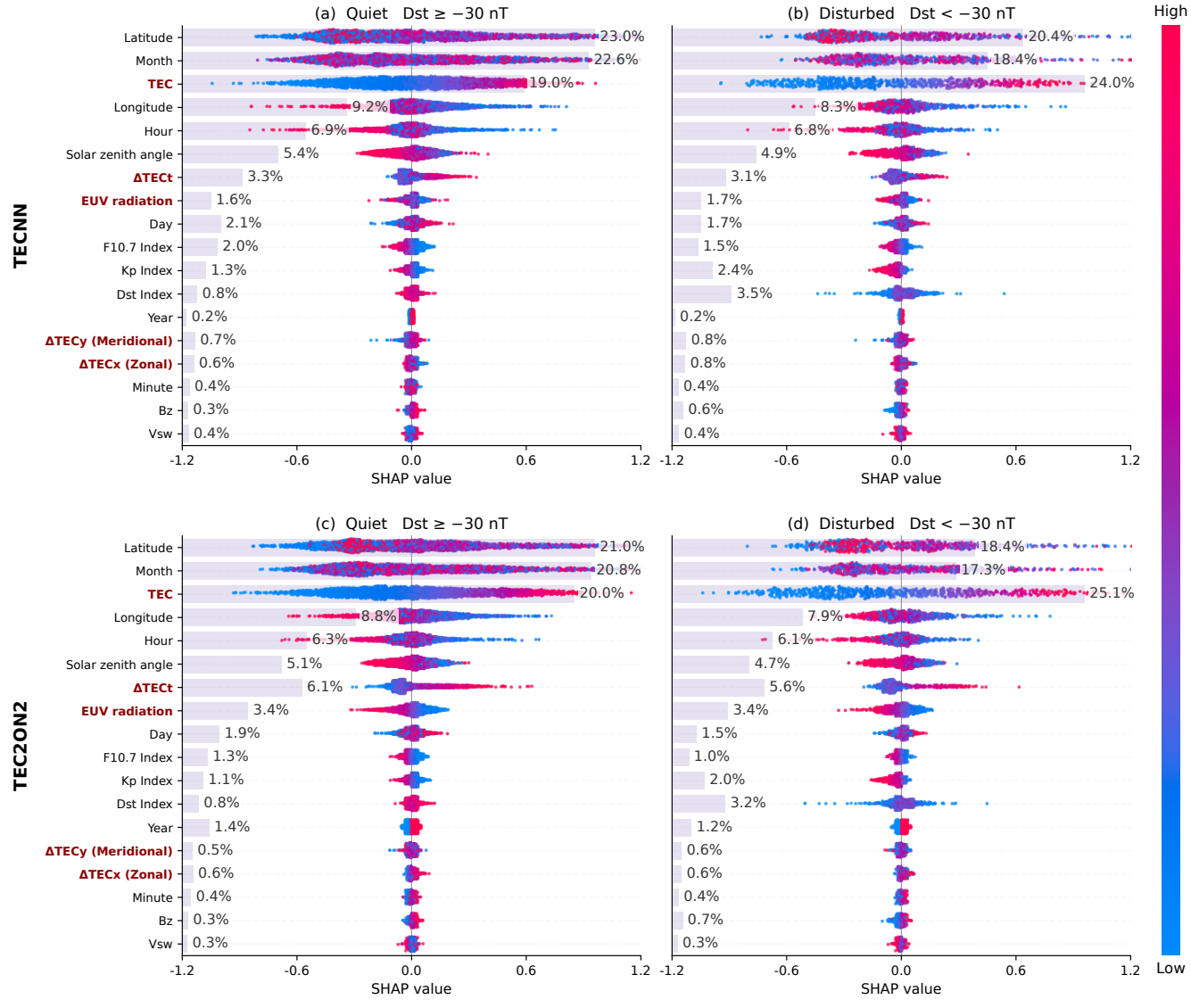

Figure 7. The SHAP-based feature importance for TECNN and TEC2ON2 on the test set.

σ_{eff} of 0.066. TEC2ON2 reduces the RMSE to 0.0708, an approximately 4.8 % reduction. The bias also decreases to -0.008, an improvement of about 77 % relative to TECNN; however, σ_{eff} increases to 0.070, representing an approximately 6 % rise. Therefore, this 4.8 % RMSE reduction is mainly achieved by correcting 77 % of the systematic bias at the cost of a 6 % increase in the random component.

Four learnable parameters are introduced in the physical branch. Because the correlation loss is invariant to α, only u, v, and γ are effectively constrained and are therefore analyzed further, as listed in Table 4. The initial values of γ, u, and v are set

https://doi.org/10.5194/egusphere-2026-6872
Preprint. Discussion started: 23 November 2026
© Author(s) 2026. CC BY 4.0 License.

Table 3. The RMSE, bias, and random component σ_{eff} of TECNN and TEC2ON2. $\langle \text{Obs} \rangle$ denotes the mean value of observed $\Sigma O/N_2$ and $\langle \text{Pred} \rangle$ is the mean value of the model predicted $\Sigma O/N_2$.

	$\langle \text{Obs} \rangle$	$\langle \text{Pred} \rangle$	RMSE	bias	σ_{eff}
Training set	0.447	—	—	—	—
Test set	0.528	—	—	—	—
TECNN	—	0.493	0.0744	−0.035	0.066
TEC2ON2	—	0.520	0.0708	−0.008	0.070

Table 4. The learned parameters over five different weight ratios. Weight ratio denotes $\lambda_1 : \lambda_2$ defined in Eq. (25).

Weight ratio	γ (h^{-1})	u (km/h)	v (km/h)
1000:1	0.4413	307.58	−76.57
100:1	0.4423	307.51	−75.71
20:1	0.4431	305.03	−74.38
10:1	0.4445	304.78	−75.06
5:1	0.4463	305.17	−76.10

to $1.6\ \text{h}^{-1}$, $100\ \text{km/h}$, and $100\ \text{km/h}$, respectively. Across the five experiments with different weight ratios, these parameters converge to the ranges of 0.4413–0.4463, 304.78–307.58 km/h, and -76.57 to -74.38 km/h, respectively. This indicates that the three coefficients recovered by the soft constraint are insensitive to the weight ratio.

Although the parameter α is not effectively constrained in our experiments, Eq. (23) shows that, with α and solar radiation fixed, the value of $\Sigma O/N_2$ depends on four terms: ΔTEC_t, $u \cdot \Delta\text{TEC}_x$, $v \cdot \Delta\text{TEC}_y$, and $\gamma \cdot \text{TEC}$. We evaluate the relative magnitudes of these four terms using all samples in the test set. The dominant term is $\gamma \cdot \text{TEC}$ (79 %), followed by ΔTEC_t (14 %), while the horizontal gradient terms collectively account for only 7 %. This observation is broadly consistent with the feature importance ranking obtained from SHAP analysis in Sect. 3.2.1.

3.3 Validation during geomagnetic storms

Many studies have demonstrated that thermospheric $\Sigma O/N_2$ exhibits global depletions during geomagnetic storms. Therefore, whether TEC2ON2 can capture the structure of $\Sigma O/N_2$ depletion during magnetic storms serves as an important indicator of the model's predictive capability under extreme space weather conditions. We next examine the reconstruction performance of TEC2ON2 during geomagnetic storms.

https://doi.org/10.5194/egusphere-2026-6872
Preprint. Discussion started: 23 November 2026
© Author(s) 2026. CC BY 4.0 License.

3.3.1 The two-dimensional $\Sigma O/N_2$ variation during geomagnetic storms

To more intuitively demonstrate whether TEC2ON2 can capture the $\Sigma O/N_2$ depletion structure during magnetic storms, we compare its reconstruction results with GOLD observations (2024–2025) and the daily-averaged products from TIMED/GUVI (2002–2007). Because absolute $\Sigma O/N_2$ values differ systematically between these datasets, we focus on relative variations rather than absolute magnitudes.

We selected two major geomagnetic storm events in 2024. One is the extreme G5 geomagnetic storm on 11 May 2024 with a minimum Dst of -406 nT, and the other is the extreme geomagnetic storm on 11 October 2024 with a minimum Dst of -333 nT. Following days of intense solar activity, active region AR3664 produced a series of seven CMEs (coronal mass ejections) toward Earth, resulting in the commencement of an extreme G5 geomagnetic storm at 17:05 UT on 10 May 2024. During this extreme G5 geomagnetic storm, NASA's GOLD successfully observed the spatial variation of $\Sigma O/N_2$ (Evans et al., 2024). Fig. 8 presents the spatiotemporal evolution of $\Sigma O/N_2$ observed by GOLD (first row), and predicted by TEC2ON2, DNN, and NRLMSIS 2.1 (second, third, and fourth rows, respectively). During 10:10–16:10, the storm was in its recovery phase, with the Dst index increasing from -297 nT to -265 nT. It can be seen from the first row of Fig. 8 that large-scale $\Sigma O/N_2$ depletion occurred in both the Northern and Southern hemispheres as observed by GOLD, and the depleted structure extended toward the vicinity of the magnetic equator. This $\Sigma O/N_2$ depleted structure is also reproduced by TEC2ON2. Although some small-scale fine structures and the magnitude of the depletion are not fully replicated, overall, the TEC2ON2 model generally reproduces the spatiotemporal evolution of the $\Sigma O/N_2$ depletion. By contrast, DNN (without physics-guided design) and the empirical NRLMSIS 2.1 fail to capture this structure.

Fig. 9 shows the $\Sigma O/N_2$ variations from GOLD observations, TEC2ON2, DNN, and NRLMSIS 2.1 during the geomagnetic storm on 11 October 2024. For this storm event, GOLD also observed large-scale depletion structures in both the Northern and Southern hemispheres. Over the Atlantic Ocean in both hemispheres, the structure mainly exhibits a shallow U-shaped pattern opening toward the polar region. TEC2ON2 also captures this large-scale depletion structure. Similarly, neither DNN nor NRLMSIS 2.1 reproduces such a structure.

For these two geomagnetic storm cases, although TEC2ON2 can well reproduce the large-scale $\Sigma O/N_2$ depletion structure observed by GOLD, discrepancies remain in the depletion magnitude and fine structures. These discrepancies may arise from two main sources. First, model error may contribute. The two extreme geomagnetic storm events in 2024 are outside the training set (their minimum Dst values are -406 nT and -333 nT, respectively). The strongest storm in the training set is the St. Patrick's Day storm (Blanchfield et al., 2025), which occurred during 16–20 March 2015 with a minimum Dst of -223 nT. This represents a typical out-of-distribution (OOD) problem. Second, GOLD observations are not taken at integer hours. The four panels correspond to universal times of 10:10, 12:10, 14:10, and 16:10, while the IGS TEC used as model input only provides 2-hourly TEC maps. We therefore approximate the inputs to TEC2ON2 using 2-hourly TEC maps at 10:00, 12:00, 14:00, and 16:00. In addition, IGS TEC is an analysis product and inherently contains deviations from true observations, and TEC and $\Sigma O/N_2$ evolve rapidly during geomagnetic storms. Consequently, 2-hourly TEC inputs may be insufficient to provide precise instantaneous information.

https://doi.org/10.5194/egusphere-2026-6872
Preprint. Discussion started: 23 November 2026
© Author(s) 2026. CC BY 4.0 License.

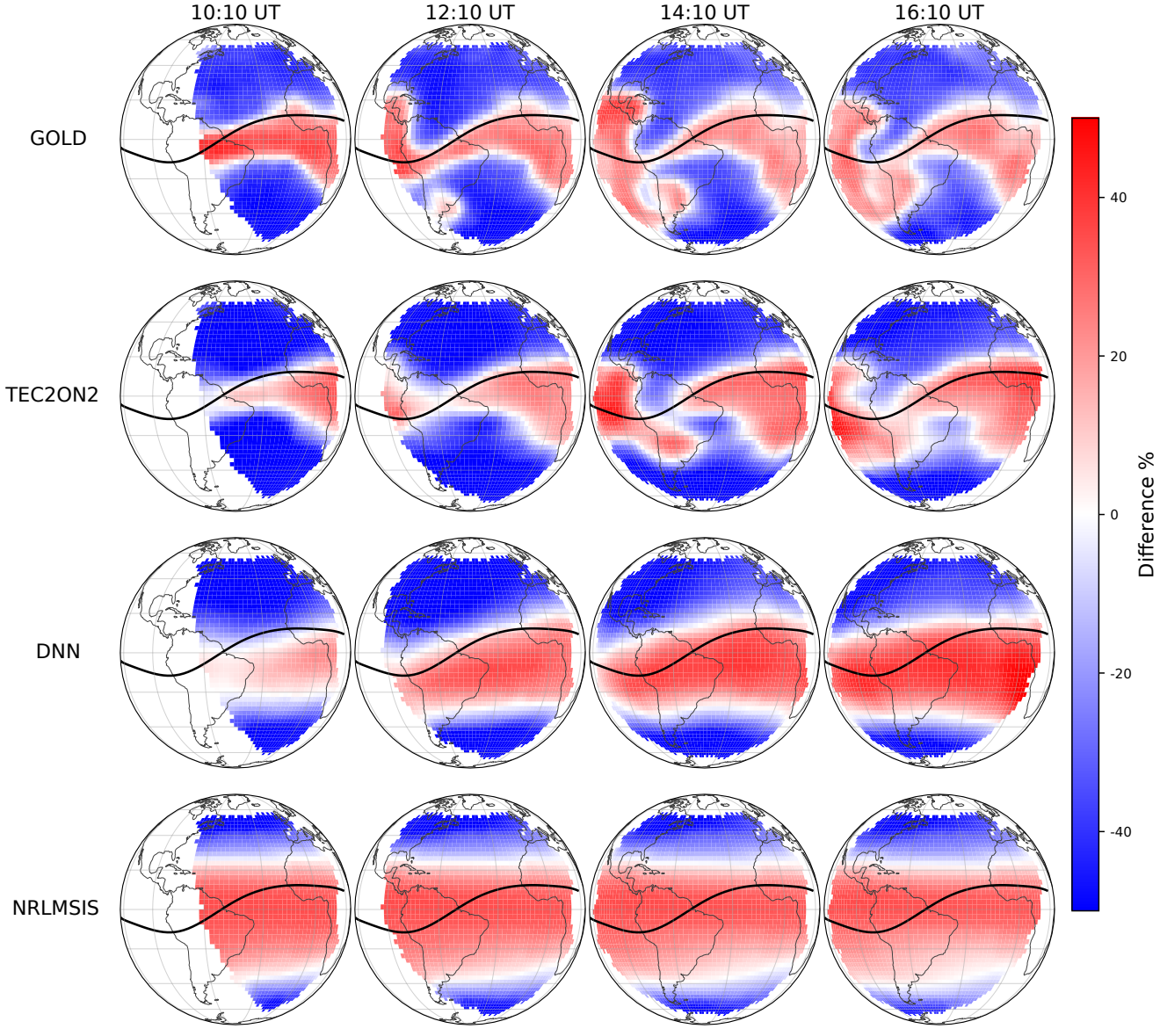

Figure 8. The spatiotemporal evolution of $\Sigma O/N_2$ from GOLD, TEC2ON2, DNN, and NRLMSIS 2.1 during 10:10–16:10 on 11 May 2024, shown as percent difference relative to the pre-storm baseline day of 9 May. Columns correspond to the four GOLD observation times and rows to GOLD, TEC2ON2, DNN, and NRLMSIS 2.1; blue/red indicate depletion/enhancement. The black line in each subplot denotes the magnetic equator.

From 2002 to 2007, GUVI provided daily-averaged global $\Sigma O/N_2$ gridded data. Although $\Sigma O/N_2$ evolves rapidly during geomagnetic storms and this daily-averaged product cannot capture its subdaily variations, storm-induced perturbations in $\Sigma O/N_2$ can still make the daily-averaged $\Sigma O/N_2$ deviate from its daily steady-state value. Therefore, we selected three extreme

https://doi.org/10.5194/egusphere-2026-6872
Preprint. Discussion started: 23 November 2026
© Author(s) 2026. CC BY 4.0 License.

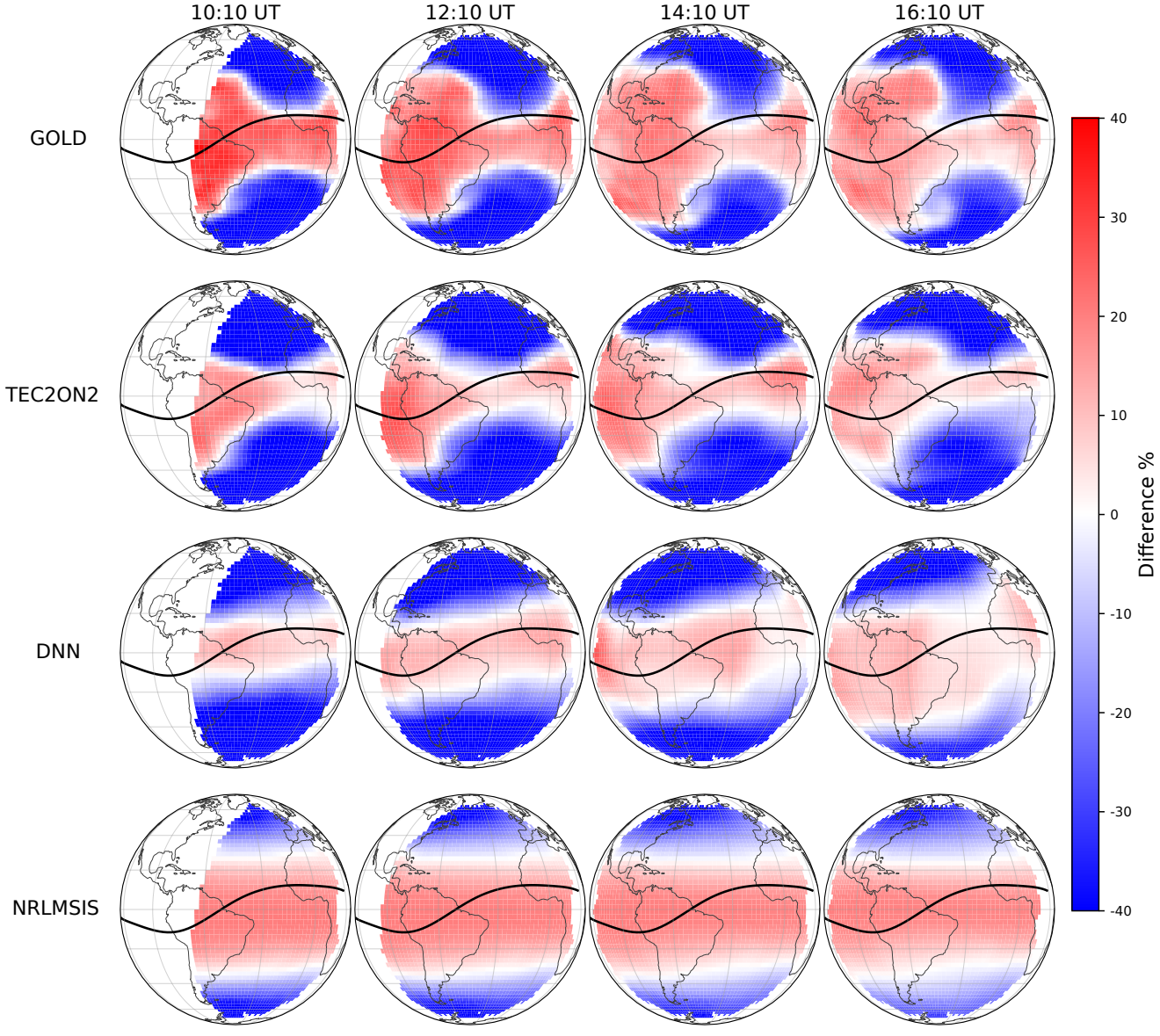

Figure 9. The spatiotemporal evolution of $\Sigma O/N_2$ from GOLD, TEC2ON2, DNN, and NRLMSIS 2.1 during 10:10–16:10 on 11 October 2024, shown as percent difference relative to the pre-storm baseline day of 10 October. The column and row layout is the same as in Fig. 8. The black line in each subplot denotes the magnetic equator.

geomagnetic storms and one weaker severe storm occurring between 2002 and 2007 to compare the performance of TEC2ON2 and GUVI daily-averaged $\Sigma O/N_2$ products during storm periods. As shown in Fig. 10, the four events exhibit clearly different $\Sigma O/N_2$ patterns in the GUVI daily grid. On 4 September 2002, the weakest of the four with minimum Dst $= -109$ nT

https://doi.org/10.5194/egusphere-2026-6872
Preprint. Discussion started: 23 November 2026
© Author(s) 2026. CC BY 4.0 License.

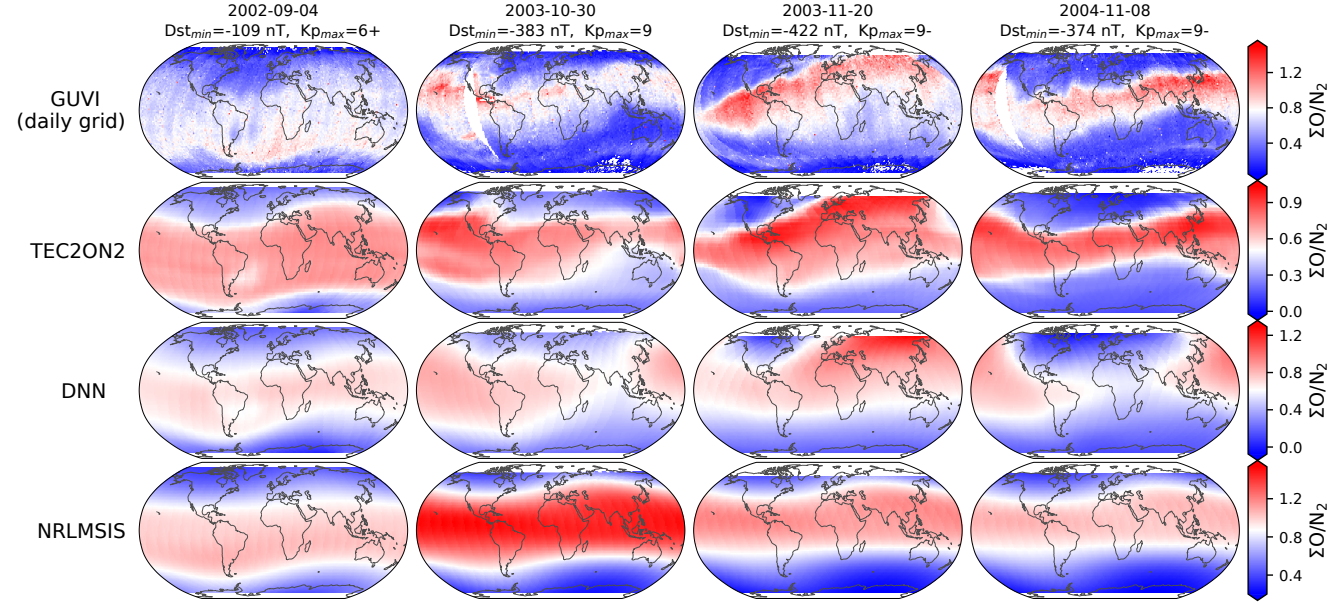

Figure 10. The spatial distribution of daily averaged $\Sigma O/N_2$ during four geomagnetic storms from TIMED/GUVI, TEC2ON2, DNN, and NRLMSIS 2.1.

(maximum Kp = 6+), the field structures of the four products are generally consistent, except that for GUVI and TEC2ON2, the lower boundary of the $\Sigma O/N_2$ depletion region lies at lower latitudes. The three extreme storms instead produce large, longitudinally coherent anomalies. On 30 October 2003 (minimum Dst = −383 nT, maximum Kp = 9), the storm-induced $\Sigma O/N_2$ depletion region extends equatorward. This depletion is most intense over the Indian Ocean northwest of Australia, and a narrow band of enhanced $\Sigma O/N_2$ forms at mid-to-low latitudes. On 20 November 2003 (minimum Dst = −422 nT, maximum Kp = 9−), the storm-induced $\Sigma O/N_2$ depletion region is mainly concentrated over North America and the Pacific Ocean to its west. Farther westward, the $\Sigma O/N_2$ low-value region shifts closer to the equator. On 8 November 2004 (minimum Dst = −374 nT, maximum Kp = 9−), extensive $\Sigma O/N_2$ depletion occurs in both the Northern and Southern Hemispheres, and a narrow band of enhanced $\Sigma O/N_2$ forms near the equator. The most pronounced equatorward extension of the depletion region in the Northern Hemisphere is observed over the Gulf of Mexico, while in the Southern Hemisphere it occurs over the Indian Ocean northwest of Australia.

For the relatively weak 4 September 2002 event the four rows are broadly similar to one another, and the differences emerge in the three extreme storms. TEC2ON2 follows the spatial structure of the GUVI daily-averaged $\Sigma O/N_2$ in all four events, while DNN and NRLMSIS 2.1 perform clearly worse, especially in the three extreme storms. TEC2ON2, however, is also smoother than GUVI and does not resolve the small-scale structure that the daily GUVI grid contains.

Overall, these geomagnetic storm cases demonstrate that TEC2ON2 can capture the large-scale $\Sigma O/N_2$ depletion structures induced by geomagnetic storms, showing reasonably good agreement with GOLD observations and TIMED/GUVI daily-

https://doi.org/10.5194/egusphere-2026-6872
Preprint. Discussion started: 23 November 2026
© Author(s) 2026. CC BY 4.0 License.



averaged products. In contrast, the DNN model without our physics-guided design and the empirical model NRLMSIS 2.1 tend to fail to reproduce such large-scale $\Sigma O/N_2$ depletion structures for the extreme storms examined here.

3.3.2 Multi-storm event validation against GOLD

In the two extreme geomagnetic storm cases above, TEC2ON2 shows better storm-time predictive capability than DNN and NRLMSIS 2.1. To systematically evaluate the performance of TEC2ON2 during geomagnetic storms, we conduct statistical analyses of the performance of each model for all geomagnetic storm events with Dst index < -100 nT from 2024 to 2025.

Because GOLD- and TIMED/GUVI-retrieved $\Sigma O/N_2$ differ systematically, we only compare the relative variations between model predictions and GOLD observations during geomagnetic storms rather than their absolute magnitudes. However, the GOLD $\Sigma O/N_2$ observations near the Equatorial Ionization Anomaly (EIA) region suffer from contamination by radiative recombination of O^+ ions, which leads to large observational errors (Qian et al., 2022). Meanwhile, models trained on TIMED/GUVI data largely fail in the SAA region. In addition, storm-induced compositional changes are generally stronger at mid-latitudes than at low latitudes. Therefore, we select the region of 20°–60°N to validate the storm-time relative variations in $\Sigma O/N_2$.

Considering the observational characteristics of GOLD, we screened on geomagnetic storm events ($\mathrm{Dst} < -100$ nT) during 2024–2025. That is, an event is retained only if GOLD provides at least two scans on that day with at least 300 valid $\Sigma O/N_2$ retrievals within 20°–60°N between 08 and 19 UT; 15 events were retained.

$$\delta\% = \frac{(\Sigma O/N_2)|_{\mathrm{storm}} - (\Sigma O/N_2)|_{\mathrm{quiet}}}{(\Sigma O/N_2)|_{\mathrm{quiet}}} \times 100\%. \tag{28}$$

Four metrics are employed to validate the performance of TEC2ON2, DNN, and NRLMSIS 2.1 against GOLD observations. All metrics are derived from the relative change $\delta\%$ (Eq. 28) evaluated at identical times and locations: the Pearson correlation coefficient between modeled and observed $\delta\%$, which measures whether the spatial pattern of the change is reproduced; the probability of detection $\mathrm{POD} = \mathrm{TP}/(\mathrm{TP}+\mathrm{FN})$ and the Jaccard index $\mathrm{TP}/(\mathrm{TP}+\mathrm{FP}+\mathrm{FN})$, which measure whether the depleted area is placed correctly; and the area under the ROC curve (AUC), obtained by using the modeled $\delta\%$ as a continuous score against the same binary GOLD label.

In this work, a depletion is defined as $\delta\% < -10\,\%$. TP (true positive) denotes the depletion detected by both model and GOLD observation; FN (false negative) represents observed depletion missed by the model; FP (false positive) represents false depletion predicted by the model that does not exist in observations.

As shown in Fig. 11, TEC2ON2 reproduces the storm-time $\Sigma O/N_2$ better than either DNN or NRLMSIS 2.1 across all four metrics. Its correlation coefficient with GOLD is 0.8, against 0.54 for DNN and 0.57 for NRLMSIS 2.1, and it scores higher in all 15 events (paired Wilcoxon, $p < 0.001$ for both comparisons). The same holds for the detection metrics: the depleted area is recovered with a POD of 0.94 and a Jaccard index of 0.69, against 0.79/0.61 (DNN) and 0.58/0.50 (NRLMSIS 2.1), and the ROC-AUC reaches 0.94 against 0.84 and 0.80. TEC2ON2 also wins the paired comparison in the Jaccard index ($p < 0.01$) and, against DNN, in the POD ($p < 0.01$).

https://doi.org/10.5194/egusphere-2026-6872
Preprint. Discussion started: 23 November 2026
© Author(s) 2026. CC BY 4.0 License.

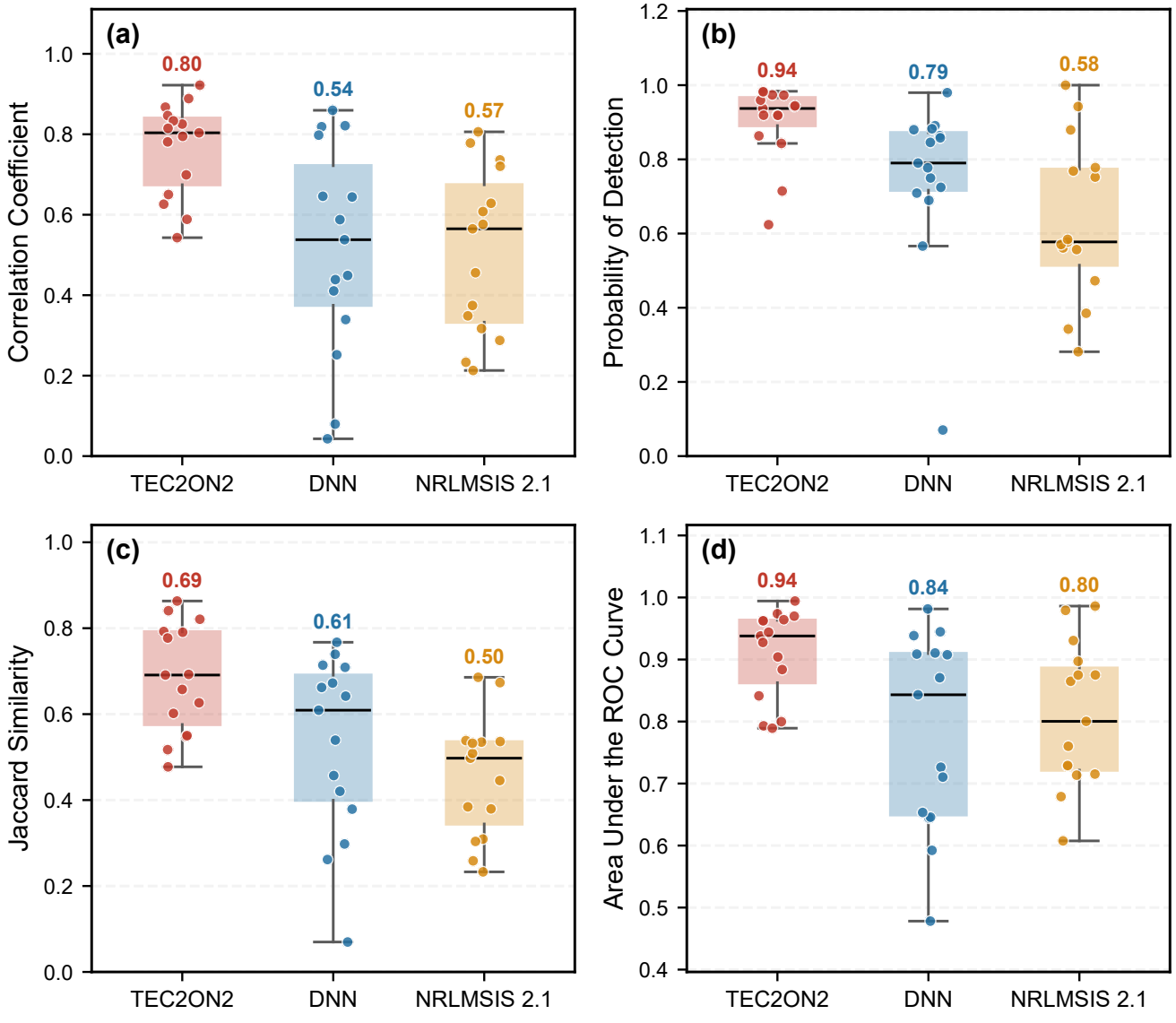

Figure 11. Distribution of the four metrics over the 15 storms of 2024–2025, evaluated over 20°–60°N: (a) correlation coefficient, (b) probability of detection, (c) Jaccard index, and (d) ROC-AUC, for TEC2ON2 (red), the DNN baseline (blue), and NRLMSIS 2.1 (orange).

Together, these metrics show that TEC2ON2 better reproduces the spatial pattern and detection of relative storm-time $\Sigma O/N_2$ depletion than the DNN and NRLMSIS 2.1 within the evaluated 20°–60°N domain.

https://doi.org/10.5194/egusphere-2026-6872
Preprint. Discussion started: 23 November 2026
© Author(s) 2026. CC BY 4.0 License.

3.4 Application in ionospheric NmF2 modeling

Previously, we developed a deep-learning model, SRON2NN, to reconstruct NmF2 in the mid- and low-latitude ionosphere using daily-averaged $\Sigma O/N_2$ data from TIMED/GUVI together with solar radiation inputs (Gong et al., 2026b). We found that $\Sigma O/N_2$ can substantially improve the reconstruction accuracy of NmF2; specifically, the RMSE decreased by 6.53 % during geomagnetic storms at mid-latitudes. However, this approach has a limitation: the daily-averaged $\Sigma O/N_2$ product cannot capture rapid variations in $\Sigma O/N_2$ during geomagnetic storms. Accordingly, we replaced the original daily-averaged $\Sigma O/N_2$ input of SRON2NN with TEC2ON2 $\Sigma O/N_2$ outputs; the updated model is hereafter referred to as SRON2NN-v2. We then compared the model metrics with those from the original SRON2NN to examine whether the $\Sigma O/N_2$ derived from TEC2ON2 is reliable and can further reduce the errors of SRON2NN.

All other configurations of SRON2NN, including the training dataset and hyperparameter settings, remain unchanged except that the daily-averaged $\Sigma O/N_2$ input is replaced with outputs fitted by the TEC2ON2 model. The full dataset was divided into training and test sets at a 9:1 ratio. The random-split experiments were repeated with ten independent random seeds to reduce the dependence on a specific partition. The results are summarized in Fig. 12.

Because the TIMED/GUVI orbital $\Sigma O/N_2$ is a dayside product with a maximum solar zenith angle of $\sim 85°$, the TEC2ON2-fitted $\Sigma O/N_2$ is unreliable above this angle. Therefore, we only replace the original daily-averaged $\Sigma O/N_2$ with $\Sigma O/N_2$ outputs from the TEC2ON2 model for solar zenith angles less than $85°$, while the original daily-averaged $\Sigma O/N_2$ values are retained for angles greater than this threshold. As shown in Fig. 12d, at different latitude bands and geomagnetic conditions, the replaced samples account for approximately half of the original samples.

Fig. 12a shows the RMSE reduction (SRON2NN-v2 relative to the original SRON2NN proposed by Gong et al., 2026b) on the test set across ten random experiments under different latitude bands and geomagnetic conditions. Fig. 12b adopts the same configuration as Fig. 12a, while the RMSE reduction is calculated using samples whose daily-averaged $\Sigma O/N_2$ values are replaced by outputs from the TEC2ON2 model. Overall, all eight latitude–geomagnetic blocks are positive in 10 out of 10 runs (two-sided Wilcoxon signed-rank test across seeds, $p = 0.002$, the smallest attainable value for ten samples), indicating that the improvement is consistent across random splits.

The reduction is not uniform across different latitude bands and geomagnetic conditions. For the samples whose $\Sigma O/N_2$ input was actually replaced (Fig. 12b), the largest reduction occurs at 30°–60°N under geomagnetically disturbed conditions ($Dst < -30$ nT), where the RMSE falls by 11.0 %, followed by 30°–60°S (7.1 %) and 0°–30°N (6.8 %), and at 0°–30°S the reduction is only 2.0 %; under quiet conditions the reduction lies between 2.20 % and 4.51 % in every band. Counting all test samples (Fig. 12a), these corresponding values decrease, e.g., from 11 % to 7.6 % at 30°–60°N under disturbed conditions, from 7.1 % to 5.1 % at 30°–60°S, and from 6.8 % to 3.7 % at 0°–30°N. This distribution is consistent with the behavior of $\Sigma O/N_2$, whose geomagnetically driven changes are stronger at mid-latitudes, with a weaker response at low latitudes.

When we further divide geomagnetic conditions into five finer Dst bins (> -20, -30 to -20, -50 to -30, -80 to -50, < -80), as illustrated in Fig. 12c, we find that the RMSE reduction increases with geomagnetic activity intensity. The maximum reduction occurs for $Dst < -80$ nT, reaching 11.0 % for the $\Sigma O/N_2$ replaced samples and 6.1 % for all test samples.

https://doi.org/10.5194/egusphere-2026-6872
Preprint. Discussion started: 23 November 2026
© Author(s) 2026. CC BY 4.0 License.

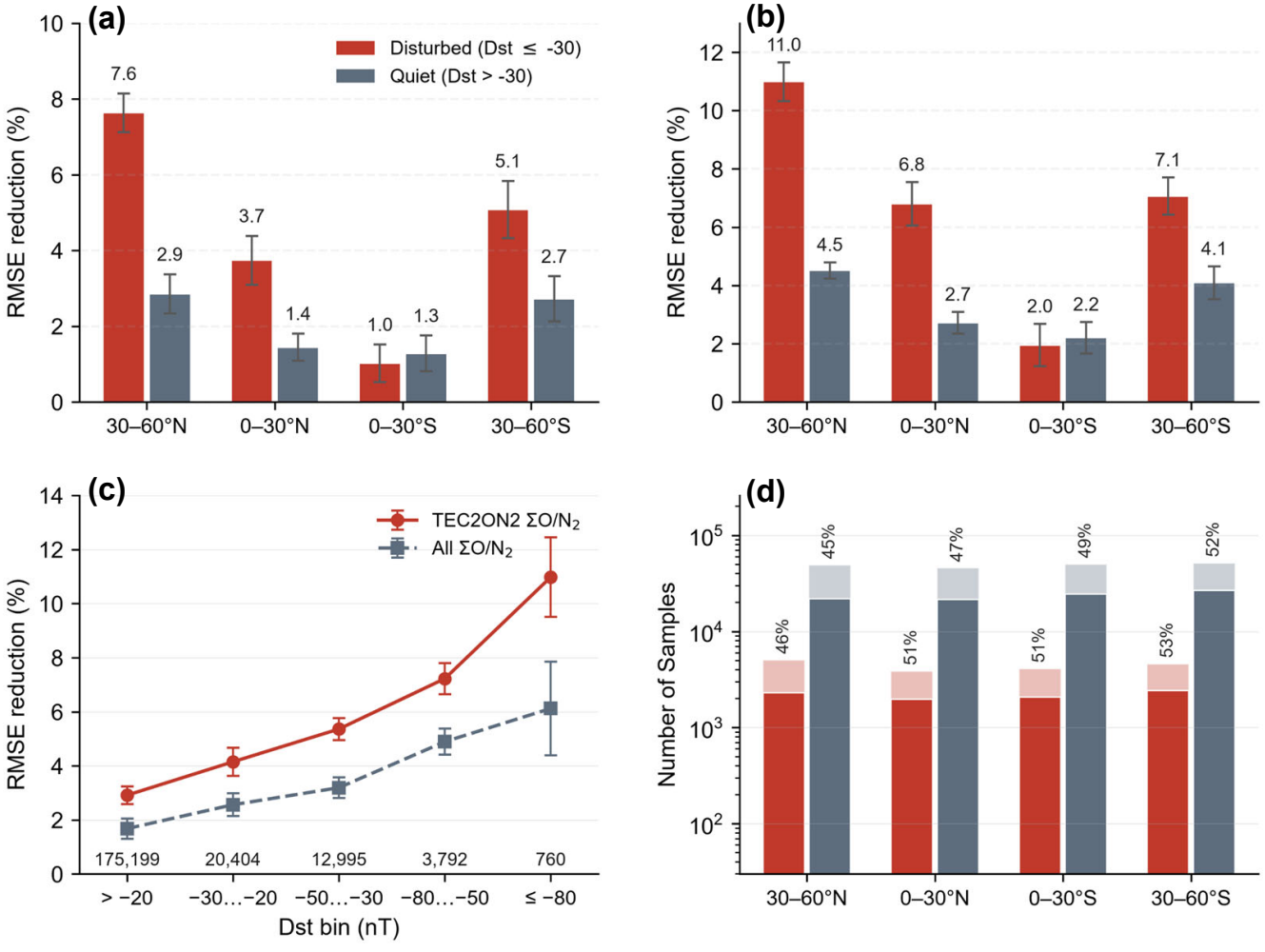

Figure 12. Overall performance of SRON2NN-v2 relative to SRON2NN. The RMSE reduction at different latitude bands and geomagnetic conditions on all test samples (a), and only TEC2ON2 replaced samples (b). (c) RMSE reduction in different Dst conditions. (d) The number of samples in each latitude band and geomagnetic condition, all samples (light shading) and, of those, the number whose $\Sigma O/N_2$ was replaced with TEC2ON2 output (solid). Error bars represent the standard deviation of RMSE reduction across 10 experiments.

These results demonstrate that the $\Sigma O/N_2$ product from TEC2ON2 improves the accuracy of ionospheric NmF2 modeling compared with the daily-averaged product from TIMED/GUVI. This also suggests that our TEC2ON2 data product is reliable.

3.5 The TEC2ON2-derived dayside $\Sigma O/N_2$ product from 1999 to 2025

The preceding results show that TEC2ON2 responds more closely to storm-time thermospheric $\Sigma O/N_2$ changes than the empirical NRLMSIS 2.1 model, and that its reconstruction agrees generally with GOLD observations during geomagnetic

https://doi.org/10.5194/egusphere-2026-6872
Preprint. Discussion started: 23 November 2026
© Author(s) 2026. CC BY 4.0 License.

storms. Over the independent test period it also matches the TIMED/GUVI orbital $\Sigma O/N_2$ with a small error. When the daily-averaged GUVI $\Sigma O/N_2$ used by the SRON2NN NmF2 model is replaced by the TEC2ON2 estimate, the NmF2 reconstruction error is further reduced. These results show that replacing daily-averaged GUVI $\Sigma O/N_2$ with TEC2ON2 output improves NmF2 reconstruction in this application, supporting the product's utility for ionospheric modeling. Therefore, we have reconstructed a dayside $\Sigma O/N_2$ product spanning the full 27-year period (1999–2025) and made it available for rapid access by the community.

The reconstruction is driven by the same inputs as TEC2ON2: the spatiotemporal coordinates (latitude, longitude, time), the IGS TEC maps, the SOHO/SEM solar EUV flux, the solar and geomagnetic indices (F10.7, Kp, Dst, V_{sw}, and B_z), and the solar zenith angle. The product is generated at every grid cell and map time of the IGS archive, so that its sampling is identical to that of the TEC input. Its spatial resolution is $2.5°$ in latitude by $5°$ in longitude, that is 71×73 cells from $87.5°$N to $87.5°$S and from $180°$W to $180°$E, with a 2-hour temporal resolution. Values are retained only for latitudes within $\pm 80°$ and solar zenith angles below $85°$, i.e., the domain in which the network was trained. Each $\Sigma O/N_2$ map is accompanied by a SAA marker, where the data suffer from large uncertainties and should be used with caution. The whole TEC2ON2 $\Sigma O/N_2$ product is available at https://doi.org/10.6084/m9.figshare.34464915 (Gong, 2026a).

4 Conclusions

This study demonstrates that GNSS TEC maps, guided by the electron continuity equation, carry sufficient information to reconstruct the global dayside $\Sigma O/N_2$ product. By embedding the continuity-equation-derived relation into both the feature design and the loss function of a deep network, the proposed TEC2ON2 framework converts a globally continuous but indirect ionospheric observation into a thermospheric composition product. The model was trained on sixteen years (2008–2023) of TIMED/GUVI orbital $\Sigma O/N_2$ observations superobbed onto $1° \times 1° \times 1$ min grids, together with IGS TEC maps and their derivatives, the SOHO/SEM 0.1–50 nm solar EUV flux, and a set of solar and geomagnetic activity indices.

On the fully independent test set of 2024–2025, which covers the maximum of Solar Cycle 25, TEC2ON2 achieves an R^2 of 0.927 and an RMSE of 0.071, reducing the RMSE by 18.1 % relative to the DNN baseline without physics-guided features or the soft constraint. Ablation experiments show that the benefit of the physics-guided features grows monotonically with geomagnetic activity, with the RMSE reduction increasing from 12.6 % under quiet conditions to 29.2 % for $\mathrm{Dst} < -100$ nT; consistently, SHAP analysis indicates that the importance share of these features rises from 25.2 % to 30.4 % from quiet to disturbed periods. The soft physical constraint further reduces the overall RMSE by 4.8 % relative to the unconstrained configuration, mainly by correcting 77 % of the systematic bias. Dedicated validations against GOLD observations and TIMED/GUVI daily-averaged products during geomagnetic storms, including the May 2024 superstorm and the 2003 Halloween storm, demonstrate that TEC2ON2 generally reproduces storm-time $\Sigma O/N_2$ depletion structures, whereas the baseline DNN and NRLMSIS 2.1 perform substantially worse. Validation of $\Sigma O/N_2$ depletion relative to quiet days across 15 storm events against GOLD observations yields a correlation coefficient of 0.8, a probability of detection of 0.94, and a ROC-AUC of 0.94, further indicating that TEC2ON2 better reproduced storm-time $\Sigma O/N_2$ depletion compared with DNN and NRLMSIS 2.1. Moreover, replacing the daily-averaged GUVI $\Sigma O/N_2$ input of our earlier SRON2NN model with the TEC2ON2 product reduces the NmF2 re-

https://doi.org/10.5194/egusphere-2026-6872
Preprint. Discussion started: 23 November 2026
© Author(s) 2026. CC BY 4.0 License.

construction error by up to 11.0 % in the replacement subset under disturbed conditions, supporting the practical value of the reconstruction for ionospheric modeling. Benefiting from the continuous availability of IGS TEC maps, we have produced and publicly released a global dayside $\Sigma O/N_2$ product covering 1999–2025 at $2.5^\circ \times 5^\circ$ spatial and 2-hour temporal resolution.

Several limitations of this work should be acknowledged. First, in the physical derivation, TEC is the altitude integral of the electron density from the bottom of the ionosphere ($h_0 \approx 60$–80 km), whereas the GUVI-retrieved $\Sigma O/N_2$ is defined above the reference altitude h_{17} at which the overhead N_2 column density reaches 10^{17} cm^{-2} (approximately 140 km). The two lower integration boundaries are treated as equivalent in our derivation; although this approximation has little impact on the leading-order relation, it introduces an inherent uncertainty into the soft physical constraint. Second, the solar forcing is represented by SOHO/SEM 0.1–50 nm flux rather than the full ionizing spectrum, so the contribution of longer-wavelength EUV emissions to the photoionization of atomic oxygen is only implicitly accounted for. Third, since the model is trained on TIMED/GUVI orbital $\Sigma O/N_2$, whose absolute magnitudes are systematically offset from those of GOLD and NRLMSIS, the significance of our reconstruction lies primarily in the spatiotemporal variability of $\Sigma O/N_2$ rather than in its absolute value. Future work will incorporate full-spectrum solar irradiance measurements and multi-mission FUV retrievals to further constrain both the magnitude and the variability of the reconstructed $\Sigma O/N_2$.

Code availability. The TEC2ON2 model code is available at https://doi.org/10.6084/m9.figshare.34464915.

Data availability. The TEC2ON2-based dayside $\Sigma O/N_2$ product (1999–2025) is available at https://doi.org/10.6084/m9.figshare.34464915 (Gong, 2026a). The TIMED/GUVI $\Sigma O/N_2$ products were obtained from https://guvitimed.jhuapl.edu/. The IGS Global Ionospheric Maps were obtained from the International GNSS Service through the NASA Crustal Dynamics Data Information System (CDDIS). The SOHO/SEM solar EUV flux data were accessed from the LASP Interactive Solar Irradiance Datacenter (LISIRD). The solar wind and geomagnetic indices (F10.7, Kp, Dst, V_{sw}, and B_z) were provided by the NASA/GSFC Space Physics Data Facility's OMNI Web service (Papitashvili and King, 2020). The GOLD $\Sigma O/N_2$ observations are available from the GOLD mission team.

Author contributions. H.G. designed the study, developed the TEC2ON2 model, and performed the analysis. H.F. supervised the study and contributed to the interpretation of the results. D.D., C.X., and C.L. contributed to the data processing and model evaluation. C.Z., J.L., H.H., and G.R. contributed to the GOLD and TIMED/GUVI data analysis. H.W. contributed to the NmF2 modeling experiment. All authors discussed the results and commented on the manuscript.

Competing interests. The authors declare that they have no competing interests.

Financial support. This research has been supported by the Innovation Research Foundation of the National University of Defense Technology.

Acknowledgements. The authors thank the Johns Hopkins University Applied Physics Laboratory for providing the TIMED/GUVI thermospheric $\Sigma O/N_2$ products (https://guvitimed.jhuapl.edu/). The authors also thank the GOLD mission team for making the GOLD $\Sigma O/N_2$ observations publicly available, and the International Association of Geomagnetism and Aeronomy (IAGA) for the IGRF-13 model.

https://doi.org/10.5194/egusphere-2026-6872
Preprint. Discussion started: 23 November 2026
© Author(s) 2026. CC BY 4.0 License.

References

Blanchfield, E. J., Carter, B. A., Currie, J. L., Weygand, J. M., and Iles, G. N.: Thermospheric density disturbances during the 2015 St. Patrick's Day geomagnetic storm: model–observation comparisons and analysis of intense polar density spikes, Space Weather, 23, e2025SW004472, https://doi.org/10.1029/2025SW004472, 2025.

Burns, A. G., Killeen, T. L., Carignan, G. R., and Roble, R. G.: Large enhancements in the O/N2 ratio in the evening sector of the winter hemisphere during geomagnetic storms, J. Geophys. Res.-Space, 100, 14661–14671, https://doi.org/10.1029/94JA03235, 1995.

Cai, X., et al.: The two-dimensional evolution of thermospheric $\Sigma O/N_2$ response to weak geomagnetic activity during solar minimum observed by GOLD, Geophys. Res. Lett., 47, e2020GL088838, https://doi.org/10.1029/2020GL088838, 2020.

Christensen, A. B., et al.: Initial observations with the Global Ultraviolet Imager (GUVI) in the NASA TIMED satellite mission, J. Geophys. Res.-Space, 108, 2003JA009918, https://doi.org/10.1029/2003JA009918, 2003.

Correira, J., et al.: Thermospheric composition and solar EUV flux from the Global-Scale Observations of the Limb and Disk (GOLD) mission, J. Geophys. Res.-Space, 126, e2021JA029517, https://doi.org/10.1029/2021JA029517, 2021.

Eastes, R. W., et al.: The Global-Scale Observations of the Limb and Disk (GOLD) mission, Space Sci. Rev., 212, 383–408, https://doi.org/10.1007/s11214-017-0392-2, 2017.

Emmert, J. T., et al.: NRLMSIS 2.1: an empirical model of nitric oxide incorporated into MSIS, J. Geophys. Res.-Space, 127, e2022JA030896, https://doi.org/10.1029/2022JA030896, 2022.

Evans, J. S., Strickland, D. J., and Huffman, R. E.: Satellite remote sensing of thermospheric O/N2 and solar EUV: 2. Data analysis, J. Geophys. Res.-Space, 100, 12227–12233, https://doi.org/10.1029/95JA00573, 1995.

Evans, J. S., et al.: GOLD observations of the thermospheric response to the 10–12 May 2024 Gannon superstorm, Geophys. Res. Lett., 51, e2024GL110506, https://doi.org/10.1029/2024GL110506, 2024.

Gong, H.: TEC2ON2 based $\Sigma O/N_2$ product and model code, figshare [data set and code], https://doi.org/10.6084/m9.figshare.34464915, 2026a.

Gong, H., et al.: Physics-motivated middle- to low-latitude NmF2 reconstruction using thermospheric $\Sigma O/N_2$ and solar EUV radiation, J. Geophys. Res.-Space, 131, e2026JA035152, https://doi.org/10.1029/2026JA035152, 2026b.

Gong, H., et al.: Physics-embedded deep learning reveals the memory effect of ionospheric electron density in response to solar EUV forcing, Geophys. Res. Lett., 53, e2026GL124459, https://doi.org/10.1029/2026GL124459, 2026c.

Hernández-Pajares, M., et al.: The IGS VTEC maps: a reliable source of ionospheric information since 1998, J. Geod., 83, 263–275, https://doi.org/10.1007/s00190-008-0266-1, 2009.

Hou, Y., Wu, M., Wang, W., Liu, X., and Guo, P.: Data fusion of ground-based GNSS, radio occultation and empirical model to predict the ionospheric peak electron density via artificial neural networks, GPS Solut., 29, 125, https://doi.org/10.1007/s10291-025-01889-7, 2025.

Immel, T. J., et al.: The Ionospheric Connection Explorer – prime mission review, Space Sci. Rev., 219, 41, https://doi.org/10.1007/s11214-023-00975-x, 2023.

Irrgang, C., et al.: Towards neural Earth system modelling by integrating artificial intelligence in Earth system science, Nat. Mach. Intell., 3, 667–674, https://doi.org/10.1038/s42256-021-00374-3, 2021.

Judge, D. L., et al.: First solar EUV irradiances obtained from SOHO by the CELIAS/SEM, Sol. Phys., 177, 161–173, https://doi.org/10.1023/A:1004929011427, 1998.

https://doi.org/10.5194/egusphere-2026-6872
Preprint. Discussion started: 23 November 2026
© Author(s) 2026. CC BY 4.0 License.



Kaselimi, M., Voulodimos, A., Doulamis, N., Doulamis, A., and Delikaraoglou, D.: Deep recurrent neural networks for ionospheric variations estimation using GNSS measurements, IEEE T. Geosci. Remote, 60, 1–15, https://doi.org/10.1109/TGRS.2021.3090856, 2022.

Kil, H., Paxton, L. J., and Schaefer, R. K.: Simultaneous detection of signatures of conjugate photoelectrons in the ionosphere and thermosphere, J. Geophys. Res.-Space, 127, e2021JA030121, https://doi.org/10.1029/2021JA030121, 2022.

Li, C., et al.: A new method for reconstruction of regional three-dimensional electron density distributions using AI-based data assimilation method and incoherent scatter radar measurements, Geophys. Res. Lett., 51, e2024GL112352, https://doi.org/10.1029/2024GL112352, 2024.

Li, L., Liu, Y., Zhou, H., Yang, K., Yan, H., and Li, J.: Ionformer: a data-driven deep learning baseline for global ionospheric TEC forecasting, IEEE T. Geosci. Remote, 63, 1–12, https://doi.org/10.1109/TGRS.2025.3542182, 2025a.

Li, Q., Fang, H., Xiao, C., Duan, D., Huang, H., and Ren, G.: Large-scale completion of ionospheric TEC maps using machine learning models with constrained conditions, IEEE J.-Stars, 18, 17092–17104, https://doi.org/10.1109/JSTARS.2025.3585566, 2025b.

Li, Z., Luan, X., Lei, J., and Ren, D.: A simulation study on the variation of thermospheric O/N2 with solar activity, J. Geophys. Res.-Space, 127, e2022JA030305, https://doi.org/10.1029/2022JA030305, 2022.

Liou, K., Newell, P. T., Anderson, B. J., Zanetti, L., and Meng, C.-I.: Neutral composition effects on ionospheric storms at middle and low latitudes, J. Geophys. Res.-Space, 110, A05309, https://doi.org/10.1029/2004JA010840, 2005.

Ma, J., Fu, H., Huba, J. D., and Jin, Y.: A novel ionospheric inversion model: PINN-SAMI3 (physics informed neural network based on SAMI3), Space Weather, 22, e2023SW003823, https://doi.org/10.1029/2023SW003823, 2024.

Meier, R. R.: The thermospheric column O/N2 ratio, J. Geophys. Res.-Space, 126, e2020JA029059, https://doi.org/10.1029/2020JA029059, 2021.

Papitashvili, N. E. and King, J. H.: OMNI daily data set, NASA Space Physics Data Facility [data set], https://doi.org/10.48322/5FMX-HV56, 2020.

Qian, L., et al.: The NCAR TIE-GCM: a community model of the coupled thermosphere/ionosphere system, in: Modeling the Ionosphere–Thermosphere System, Geophysical Monograph Series, edited by: Huba, J., Schunk, R., and Khazanov, G., Wiley, 73–83, https://doi.org/10.1002/9781118704417.ch7, 2014.

Qian, L., Gan, Q., Wang, W., Cai, X., Eastes, R., and Yue, J.: Seasonal variation of thermospheric composition observed by NASA GOLD, J. Geophys. Res.-Space, 127, e2022JA030496, https://doi.org/10.1029/2022JA030496, 2022.

Raissi, M., Perdikaris, P., and Karniadakis, G. E.: Physics-informed neural networks: a deep learning framework for solving forward and inverse problems involving nonlinear partial differential equations, J. Comput. Phys., 378, 686–707, https://doi.org/10.1016/j.jcp.2018.10.045, 2019.

Richmond, A. D., Ridley, E. C., and Roble, R. G.: A thermosphere/ionosphere general circulation model with coupled electrodynamics, Geophys. Res. Lett., 19, 601–604, https://doi.org/10.1029/92GL00401, 1992.

Schunk, R. W. and Nagy, A. F.: Ionospheres: Physics, Plasma Physics, and Chemistry, 2nd edn., Cambridge Atmospheric and Space Science Series, Cambridge University Press, Cambridge, 2018.

Strickland, D. J., Evans, J. S., and Paxton, L. J.: Satellite remote sensing of thermospheric O/N2 and solar EUV: 1. Theory, J. Geophys. Res.-Space, 100, 12217–12226, https://doi.org/10.1029/95JA00574, 1995.

Sui, Y., et al.: Multilayer ionospheric model constrained by physical prior based on GNSS stations, IEEE J.-Stars, 16, 1842–1857, https://doi.org/10.1109/JSTARS.2023.3241321, 2023.

https://doi.org/10.5194/egusphere-2026-6872
Preprint. Discussion started: 23 November 2026
© Author(s) 2026. CC BY 4.0 License.



Sui, Y., Fu, H., Xu, F., and Jin, Y.-Q.: Global ionospheric tomography based on data-driven fusion algorithm using GNSS, IEEE Geosci. Remote S., 21, 1–5, https://doi.org/10.1109/LGRS.2024.3441632, 2024.

Tang, J., Zhong, Z., Ding, M., Yang, D., and Liu, H.: Forecast of ionospheric TEC maps using ConvGRU deep learning over China, IEEE J.-Stars, 17, 3334–3344, https://doi.org/10.1109/JSTARS.2024.3349392, 2024.

Tulasi Ram, S., Sai Gowtam, V., Mitra, A., and Reinisch, B.: The improved two-dimensional artificial neural network-based ionospheric model (ANNIM), J. Geophys. Res.-Space, 123, 5807–5820, https://doi.org/10.1029/2018JA025559, 2018.

Verkhoglyadova, O. P., Tsurutani, B. T., Mannucci, A. J., Mlynczak, M. G., Hunt, L. A., and Paxton, L. J.: Ionospheric TEC, thermospheric cooling and $\Sigma[O/N_2]$ compositional changes during the 6–17 March 2012 magnetic storm interval (CAWSES II), J. Atmos. Sol.-Terr. Phy., 115–116, 41–51, https://doi.org/10.1016/j.jastp.2013.11.009, 2014.

Xia, P., Xie, X., Zhang, L., Chen, B., and Guo, M.: Real-time inversion of ionospheric electron density profiles from single-station GNSS based on LSTM networks, IEEE T. Geosci. Remote, 64, 5802217, https://doi.org/10.1109/TGRS.2026.3715243, 2026.

Yang, F., Li, W., Li, J., Zuo, X., Zhao, D., and Zhang, K.: Spatiotemporal implicit neural representation for ionospheric tomography with multi-LEO occultation data, IEEE T. Geosci. Remote, 64, 1–16, https://doi.org/10.1109/TGRS.2026.3667515, 2026.

Zhang, Y. and Paxton, L. J.: Long-term variation in the thermosphere: TIMED/GUVI observations, J. Geophys. Res.-Space, 116, A02302, https://doi.org/10.1029/2010JA016337, 2011.

Zhang, Y., Paxton, L. J., Morrison, D., Marsh, D., and Kil, H.: Storm-time behaviors of O/N2 and NO variations, J. Atmos. Sol.-Terr. Phy., 114, 42–49, https://doi.org/10.1016/j.jastp.2014.04.003, 2014.